

Performance of the MICE diagnostic systems

5

A.N. Other et al.

Abstract

This paper will describe:

- The detectors as we have it installed in the MICE Hall at November 2017
- The performances of the detectors and the PID
- The absorbers model(s) and their validation
- The track matching
- The detector alignment

10

Reference to the published papers. Target: JINST volume.

Table 1: Status of the paper

Contribution	Plots	Text
TOF	Second version	First version
Cherenkov	First version	First version
KL	First version	First version
EMR	First version	First version
Tracker	Some	Introduction
PID	No	No
Track matching	First version	First version
Detector alignment	First version	First version
Absorber model	Draft	Draft

Contents

15	1 Introduction	2
	2 Time-of-Flight Detectors	2
	2.1 Introduction	2
	2.2 Calibration Method	4
	2.3 Reconstruction	7
20	2.4 Performance	8
	3 Cherenkov Detectors	10
	3.1 Introduction	10
	3.2 Performance	10
	4 KLOE-Light Calorimeter	13
25	4.1 Introduction	13
	4.2 Performance	13

5	Electron Muon Ranger	16
30	5.1 Introduction	16
	5.2 Performance	17
6	The Trackers	24
35	6.1 Introduction	24
	6.2 Tracker Performance and Reconstruction	25
	6.3 Tracker Efficiency Evolution	26
7	PID	27
35	7.1 Introduction	27
	7.2 Performance of the PID	27
8	Track Matching	27
40	8.1 Global reconstruction	27
	8.2 Beam based magnet alignment	35
9	Beam-based detector alignment	35
40	9.1 Introduction	36
	9.2 Analysis method	37
	9.3 Alignment of a data sample	41
	9.4 Propagation	42
10	Absorber	45
45	10.1 Absorber vessel body	47
	10.2 Windows	49
	10.3 Validation of the absorber model in MAUS	52
11	Conclusions	52

50 **1 Introduction**

To include:

- Motivation
- Outline of the experiment

2 Time-of-Flight Detectors

55 **2.1 Introduction**

Three time-of-flight detectors (TOF0, TOF1, TOF2) were built and installed at RAL in 2008 and 2009 to measure the position and the time of crossing particles. TOF0 and TOF1 [1], [2], [3] were placed upstream of the cooling channel, and TOF2 [4] was downstream of the channel, mounted in front of the KL, as shown in Fig. 1. The time of flight between two TOF stations provides particle identification information and can also be used for momentum measurement. TOF1 served most of the time also as an experimental trigger. They operated smoothly during the so-called Step I and Step IV [5], [6] running periods of the MICE experiment and were essential for all the measurements done.

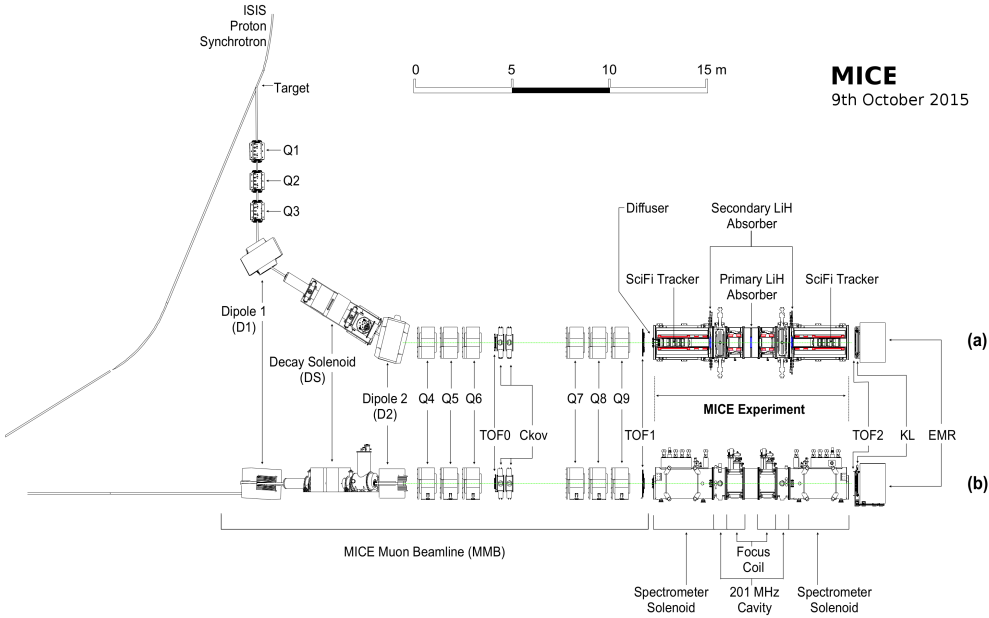


Figure 1: MICE experiment in the demo configuration, showing the full beam line and cooling channel elements with all the detectors.

The good performances of the TOF detectors, over an extended period of time, enabled the MICE experiment to characterize fully its muon beams during Step I data-taking, by measuring their emittance [7] and assessing their pion contamination [8].

Each TOF station was made of two planes of fast 1" thick scintillator bars oriented along X and Y directions, respectively. The bars were made of BC404 plastic scintillator¹. A simple fishtail light-guide was used to attach each end of a bar to R4998 Hamamatsu fast photomultiplier tubes². R4998 PMTs were delivered by Hamamatsu in assemblies (H6533MOD) that included the PMT tube, the voltage divider chain and a 1 mm thick μ -metal shield, extending 30 mm beyond the photocathode surface. To increase the count rate stability active dividers were used, instead of conventional resistive ones. Illustration of TOF1 station is shown in Figure 2 together with an exploded view of a slab.

The stations TOF0, TOF1, and TOF2 had active areas of $40 \times 40 \text{ cm}^2$, $42 \times 42 \text{ cm}^2$, and $60 \times 60 \text{ cm}^2$ respectively. Each of the planes in TOF0 station had 10 4-cm wide scintillator slabs. Stations TOF1 and TOF2 used 7 and 10 in each plane, respectively.

The PMTs are connected to a 50% – 50% passive splitter using $\sim 34 \text{ m}$ long RG213 signal cable. One half of the signal is fed to the leading-edge CAMAC Lecroy 4115 discriminator followed by CAEN V1290 TDC for time measurements. Second half of the signal goes to CAEN V1724 FADC for pulse-height measurements. Pulse height measurement is instrumental for time-walk corrections. Each station issued a local readout trigger if signals in both PMTs attached to a slab crossed a specific threshold. All three stations were read out when TOF1 station issued a local trigger. This readout trigger was also used for the rest of the MICE detector systems.

All stations were exposed to residual magnetic fields: TOF0 station was placed in a relatively low residual field produced by the last quadrupole magnet of the beam line, while the other two TOF stations were exposed to the stray fields of the cooling channel solenoids. A shielding structure was adopted covering all PMTs at each side of the stations. Fig. 3 shows photographs from the assembly of the TOF2 station at INFN MIB, taken

¹Emission maximum at 408 nm, decay time 1.8 ns, attenuation length 160 cm

²one-inch linear focused PMTs with 10 stages, typical gain $G \sim 5.7 \times 10^6$ at -2250 V and $B=0$ T, rise time 0.7 ns, transit time spread (TTS) ~ 160 ps

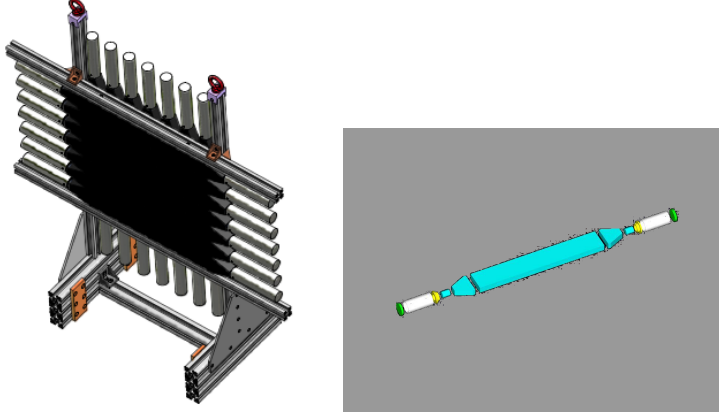


Figure 2: TOF design [9] and slab components [2].



Figure 3: Assembly of TOF2 at INFN MIB mechanics workshop. Left to right: from the bare magnetic shielding to the fully assembled counters of one plane.

from [4].

The purpose of the TOF system is to effectively discriminate particle species based on time-of-flight measurement. The main components in the MICE beam are muons, pions, and electrons. The time resolution needs to be sufficiently good to effectively discriminate between these types. At 240 MeV/c, the time-of-flight difference between muon and pion is about 1.3 ns between TOF0 and TOF1 stations. With 200 ps resolution, one reaches near 100% discrimination efficiency.

2.2 Calibration Method

Measurement of time traversal of a particle through a TOF station is influenced by several factors at the hardware level. When a particle crosses the plastic scintillator, there is a short delay in light production, with a characteristic decay time of 1.8 ns.

After generation, scintillation light propagates to the ends of each scintillator slab where it is detected by photomultiplier tubes. The light-travel time depends on the distance of the particle crossing from the PMT. The lengths of slabs in TOF0, TOF1, and TOF2 were 40 cm, 42 cm, and 60 cm, respectively. This translates to about 3 ns, 3.1 ns, and 4.4 ns, respectively, as the effective light propagation speed in the scintillator was found to be approximately 13.5 cm/ns.

More delay was introduced by the transit time of each PMT and of the cable that led the signal to the readout electronics. These times were unique for each individual PMT channel and needed to be determined in dedicated measurements.

The times of each signal of a PMT were measured as times of signal threshold crossings in a simple linear discriminator. This introduced bias in the measured time dependent on the total charge of the signal, effect

referred to as time-walk.

Signal times of each channel were recorded in TDC boards. Readout of the whole system was triggered by having a signal in TOF1 station. The readout trigger signal is distributed to all TDC boards and is used as a reference time. Which PMT channel's threshold crossing caused the readout was depending on where the particle crossed through the TOF1 station. As a consequence, the reference time had a bias dependent on the position of TOF1 crossing, an effect referred to here as trigger delay.
110

The final time measurement in each station was determined as an average of the times of individual channels. This way, different distance from the point of crossing to each side of the scintillator slabs does not matter anymore, because the average of the times of the 2 PMTs does not depend on it.

115 Corrections which need to be made to the measured times are then the time-walk correction, the PMT channel specific delay time T_0 , and a correction for the reference trigger time delay.

Details of the calibration method are described in [10].

2.2.1 Time-walk Correction

First correction to the measured time of each channel is time-walk correction. It was considered to be a static
120 property of each channel. The same correction was used for all runs. The correction was determined by looking at time difference between two selected channels of slabs from different planes.

Let T^{ijk} denote a TDC measured time in PMT k of a slab j in a plane i . Similarly, let ADC^{ijk} be the measured pulse height in that PMT channel. Then time-walk of PMT k in slab j of plane 0 was determined from the 2D distribution of $T^{14k'} - T^{0jk}$ vs. ADC^{0jk} . The reference channel was chosen from slab in the
125 middle of the other plane (slab 4 in this example). PMT with higher mean ADC count was selected.

A special pre-correction was first determined for reference slabs, middle slabs in each plane. Only events where particle crossed the pixel corresponding to their crossing were considered. The pixel was in the centre of the station and was always well populated with particles crossing it. The ADC count in one of the slabs taken as a reference was limited to a 10% region around its mean. The TDC time of the slab was then little affected
130 by the time walk.

The following function was fitted to the profile of the 2D data histogram:

$$f(ADC) = P_1 + \frac{P_2}{ADC - P_0} + \frac{P_3}{(ADC - P_0)^2}. \quad (1)$$

Where possible, parameter P_3 was fixed to 0. For some PMTs such fit would not follow the measured trend and the additional parameter was added to the fit.

After the pre-correction of the reference slabs, time-walk of all the PMT channels was determined by looking at events in pixels corresponding to the crossing with the reference slab.

135 An example of time walk of a channel with respect to pre-corrected time in a reference slab is shown in Figure 4. The residual effect of time walk after the correction is also shown.

Figure 5 shows distributions of time differences between horizontal slab 4 and vertical slab 5 before and after the time-walk correction. The width of the distribution is significantly decreased. The mean of the distribution is not centered at 0 as differences in delays T_0 were not accounted for, yet.

140 2.2.2 Trigger Delay Correction

Station TOF1 was used to trigger the readout of the whole system. Time of it's trigger signal was used as a reference signal for time measurements of all 3 stations. Depending on position where a particle was crossing the TOF1 station, this trigger signal will have different delays. The delay of each pixel was measured relative

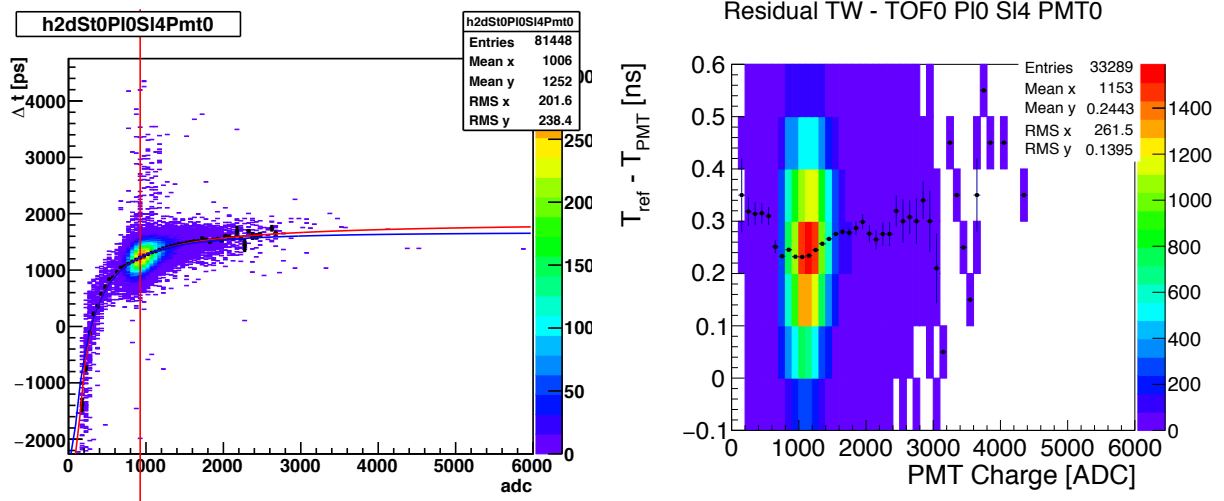


Figure 4: Time walk (left) in PMT 0 of slab 4 in plane 0 (horizontal) of station TOF0. The 2D histogram (coloured scale) is overlaid with its profile and with the fit function described in Equation (1). Residual time walk (right) after the correction was applied.

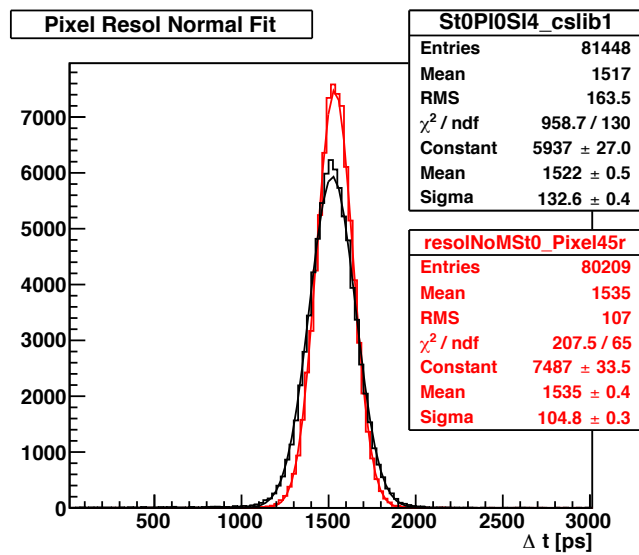


Figure 5: Distribution of time differences ΔT between horizontal slab 4 and vertical slab 5 in station TOF0. Distribution before and after the time-walk correction are overlaid.

to the central pixel of TOF1 station. It was assumed that the source of the delay for individual pixel did not
145 change from event to event. Although in reality this was not the case for most of the pixels, it was a good enough approximation.

Determination of the trigger delays for each pixel was as follows: Times of each PMT were corrected for time walk first. Trigger delay of the central pixel, defined as a crossing of station's 2 reference slabs, was set to 0. Trigger delays of the rest of the pixels in the reference slabs were calculated from differences of mean
150 times of each PMT. For example, for pixels i of the horizontal reference slab refx, the trigger delay time $T_{\text{refx},i}^{\text{trig}}$ is given by:

$$T_{\text{refx},i}^{\text{trig}} = \frac{1}{2} \sum_{\text{PMT}} \left\langle t_{\text{refx},i}^{\text{PMT,refx}} \right\rangle - \left\langle t_{\text{refx,refy}}^{\text{PMT,refx}} \right\rangle, \quad (2)$$

where $t_{i,j}^{\text{PMT},i}$ is the time in PMT of slab i for events where particle crossed pixel i, j . The delays are averaged over both PMTs of the slab. Pixel denoted refx,refy is the central reference pixel of the TOF1 station.

For the rest of the pixels, not defined by the reference slabs, the trigger delay times were determined as a
155 delay with respect to the pixels on the reference slabs. Delays of those reference pixels were then added:

$$T_{i,j}^{\text{trig}} = \frac{1}{4} \sum_{\text{PMT}} \left(\left\langle t_{i,j}^{\text{PMT},i} \right\rangle - \left\langle t_{i,\text{refy}}^{\text{PMT},i} \right\rangle + \left\langle t_{i,j}^{\text{PMT},j} \right\rangle - \left\langle t_{\text{refy},j}^{\text{PMT},j} \right\rangle \right) + \frac{1}{2} \left(T_{i,\text{refy}}^{\text{trig}} + T_{\text{refx},j}^{\text{trig}} \right) \quad (3)$$

2.2.3 T_0 Correction

Times in each channel were also corrected for the channel specific delays caused by each PMT and by the cable lengths. The correction was determined from times measured of particles crossing through the middle pixel of each slab. The times were corrected for the time walk and for TOF0 and TOF2 stations also for the trigger
160 signal delay. The correction for TOF1, the readout triggering station, were set such that the mean of the time distribution was at 0.

Times in TOF0 and TOF2 stations reflected the time of flight of individual particles to and from TOF1. Distribution of the times in those stations show 3-peaked structure, where the most isolated peak at lowest time-of-flight corresponds to the electrons. They travel at the speed of light and their time of flight was calculated
165 from distances from TOF1 station. Corrections for each channel were determined such that the electron peak was located at the predicted time of flight.

Figure 6 shows position of the electron peak as measured by TOF0 station in one run with beam at nominal 140 MeV/c. Uncorrected raw times are compared to fully corrected time. Corrected-time distribution shows better electron peak separation and it also places it to the correct position relative to TOF1.

170 Due to the presence of focusing fields in the beam-line section between TOF0 and TOF1 stations, particles did not travel in a straight line in that section. Deviation from a straight line was dependent on the initial direction and momentum of the particles entering the section. The effect was estimated [9] in simulations to be of an order of ~ 30 ps. This effect caused a small bias in the calibrations.

2.3 Reconstruction

175 Particle crossing a TOF station must have crossed 2 orthogonal slabs in the stations 2 planes. The time and approximate position of particle crossing a TOF station was reconstructed from the PMT signals in the two slabs. Each slab with at least one recorded signal in each of the 2 attached PMTs was considered as being crossed by a particle. Times of these recorded signals were corrected for time-walk, readout trigger signal delay, and the channel specific delay. Time of crossing of the slab was then taken as the average of the 2
180 corrected PMT times.

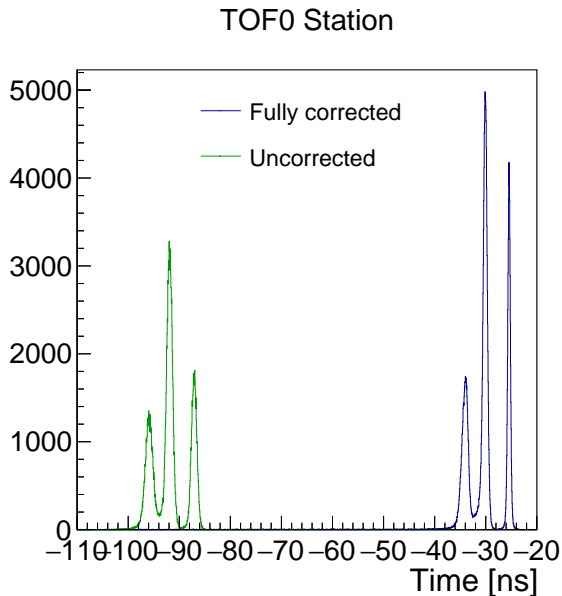


Figure 6: Example of time distribution of events in TOF0. Times before any corrections are compared to to times with all corrections applied.

The 2 slabs hit by a particle defined a pixel of area given by the width of the slabs. Sometimes, there were more slabs in each plane with signals. Matching of 2 slabs being crossed by a particle was done based on their measured signal time. They were matched if the times were within a 4-ns window. The time of the particle crossing was determined as the average of times of the 2 matched slabs.

In order to be able to correct for the trigger signal delay, the pixel through which the particle crossed TOF1 needed to be determined. All possible combinations of 2 slabs from 2 different planes were tested. The times of the recorded PMT signals were corrected under the hypothesis that correct slabs were matched. The pixel of the crossing particle was identified if the time difference of the 2 slabs was shorter than 4 ns.

2.4 Performance

Resolution of time-of-flight measurement is given by time resolution of each station. The time of a station particle crossing is determined from the average of times of the two slabs. The resolution of the average is a half of the spread of their difference. Therefore, looking at slab ΔT allows determination of the time-of-flight resolution.

Due to the errors in calibrations, especially in the underpopulated peripheral pixels, the slab ΔT distributions have slight offsets from 0. Also, the spread of the distributions varies from pixel to pixel. The offsets and the spreads of the slab ΔT distributions for individual pixels are shown in Figures 7 and 8, respectively.

Overall performance can be inferred from the combined slab ΔT distributions. The plots in Figure 9 show that they all centre approximately at 0 ns and they exhibit very similar resolutions, with TOF1 having the largest spread.

The reconstruction of a pixel by matching of 2 slabs from different planes of each station is dependent on the slab ΔT . The 4 ns time window for the matching was chosen to cover the errors of the calibrations. Yet, there were times when there were signals in slabs in each plane of a station, but they were never matched. These events were mostly results of multiple particles passing through the station and causing signal in one plane only. They would never be matched in time as they arrived within the beam bunch time stretch of about

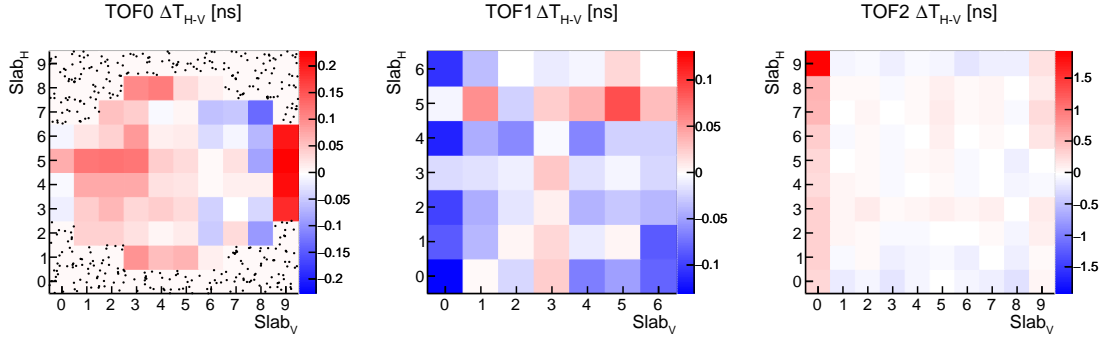


Figure 7: Offsets in slab ΔT for individual pixels for all 3 stations.

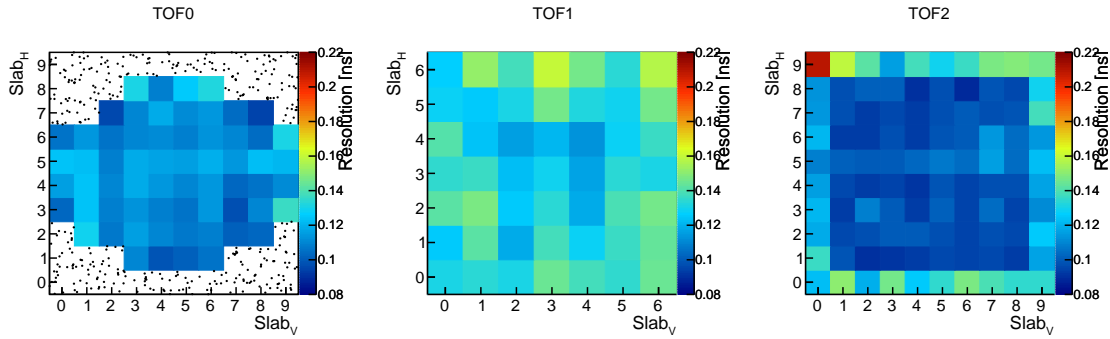


Figure 8: Spread in the slab ΔT distributions of each pixel.

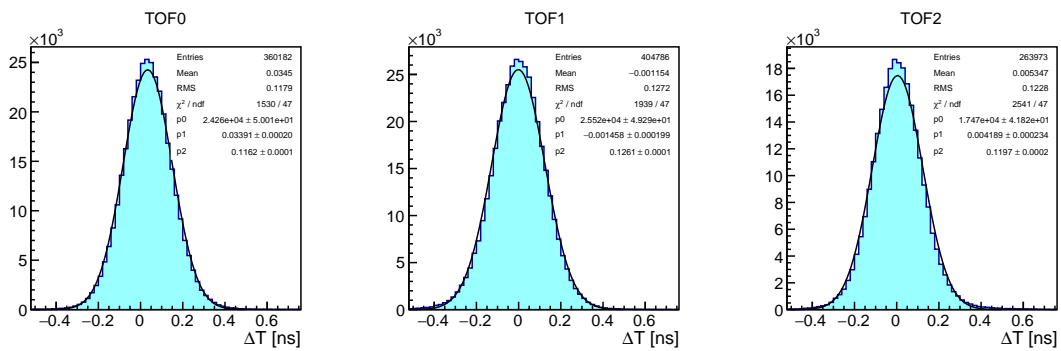


Figure 9: Overall slab ΔT distributions. Total width of the distribution is due to the resolution of individual pixels and due to the offsets in their ΔT distributions.

205 1 μ s. Figure 10 shows fractions of events where there were signals in two perpendicular slabs and they were time-matched. One can see lower efficiency/fraction in the peripheral pixels which is associated with the larger fraction of multiple particle crossings with giving signal in one slab only.

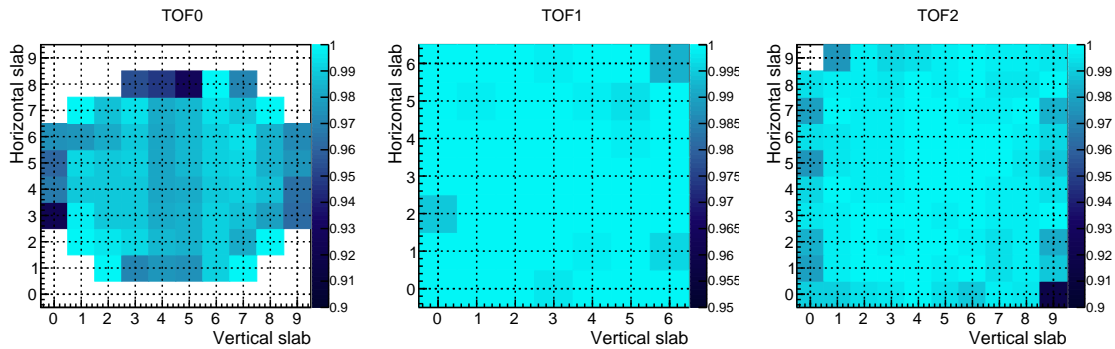


Figure 10: Efficiency of space point creation if there were hits in two transverse slabs.

3 Cherenkov Detectors

3.1 Introduction

210 The MICE Cherenkov threshold detectors, measuring velocity, are primarily designed to provide π - μ separation in the higher momentum ranges, where TOF peaks separation is not sufficient for conclusive particle identification.

215 In order to provide separation over a large range of momenta, two high density silica aerogel Cherenkov detectors (CkovA and CkovB) with refractive indices $n=1.07$ and $n=1.12$ are used. Light is collected in each counter by four 9354KB eight-inch UV-enhanced phototubes and recorded by CAEN V1731 FADCs (500 MS/s). The two detectors are placed directly one after another in the beamline, located just after the first TOF counter. In Fig. 11 an exploded view of one detector is shown.

220 Their respective thresholds provide different responses in four distinct momentum ranges, i.e. in the 200 MeV/c beams, pions are below the threshold which would fire the detector for both CkovA and CkovB whereas muons are above only for CkovB, while for the 240 MeV/c beams, pions are above the threshold for CkovB while muons are above for both CkovA and CkovB. Using this information algorithms can be written that produce likelihood distributions of particle type. Below the CkovB muon threshold of about 217.9 MeV/c, where there is no separation, the TOFs provide good separation, whereas the momentum range above the CkovA pion threshold 367.9 MeV/c is outside of the MICE running parameters [11]. For unambiguous identification 225 of particle species the Cherenkov detectors would need a momentum measurement from the MICE Tracker.

3.2 Performance

The data sets used to evaluate the Cherenkov detectors are summarized in Table 2. A wide range of settings (including alignment runs) has been used in order to cover the full spectra of particles that could have been measured by the detectors.

230 The asymptotic light yield (for $\beta=v/c=1$) in each counter has been measured using the electron peaks, giving 16 ± 1 photoelectrons (NPE) in CkovA and 19 ± 1 in CkovB.

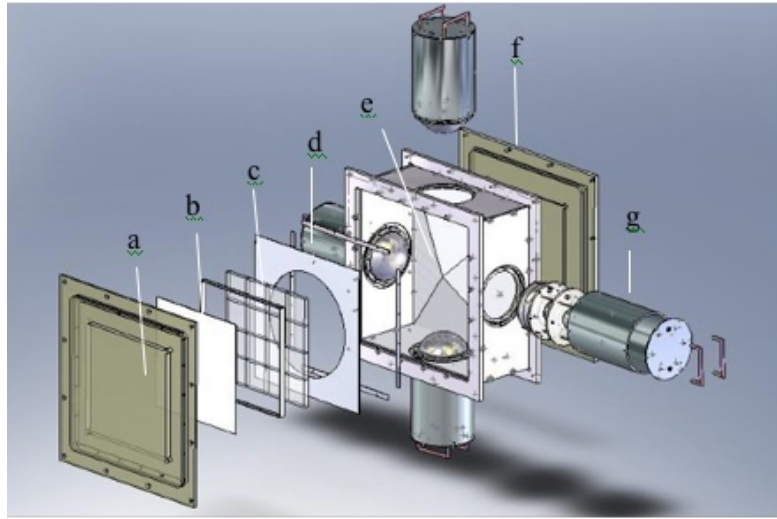


Figure 11: MICE aerogel Cherenkov counter blowup: a) entrance window, b) mirror, c) aerogel mosaic, d) acetate window, e) GORE reflector panel, f) exit window and g) eight-inch PMT in iron shield.

Run ID	Date	Nominal momentum [MeV/c]	Spills	Triggers
10488	12/12/2017	140	3777	300269
10496	12/12/2017	170	4180	371037
10391	03/12/2017	200	2146	240033
10419	04/12/2017	240	2932	328062
10304	29/11/2017	300	2502	305363
10221	23/11/2016	300	4493	560119
10519	15/12/2017	400	4316	506384

Table 2: Summary of the data sets used to visualize the activation curve of the MICE Cherenkov detectors.

The photoelectrons yields versus momentum for muons and pions in CkovA and CkovB are displayed in Fig. 12, using the time of flight between TOF0 and TOF1 to select the species and estimate the momenta. The distributions of NPEs as a function of the momentum P have been fitted with the function

$$NPE(P) = NPE_0 + NPE_{\beta=1} \left(1 - \left(\frac{P_0}{P} \right)^2 \right) \quad (4)$$

where NPE_0 is the number of background photoelectrons, $NPE_{\beta=1}$ is the asymptotic light yield and P_0 is the momentum threshold.

The observed muon thresholds are 267.2 ± 5.2 and 220.0 ± 16.9 MeV/c, while for pions are 331.8 ± 16.4 MeV/c and 296.1 ± 0.1 MeV/c, respectively in CkovA and CkovB. The $NPE_{\beta=1}$ values are generally lower than the values predicted as in a previous analysis [11] done with Step I data: this is mostly due to TOF0 acting as a pre-shower radiator.

In Fig. 13 is shown the typical photoelectron spectra for muons and pions well above the threshold. The expected Poisson-like distribution got tails from the electromagnetic showers and from secondary electrons coming from interactions in TOF0 and in the aerogel itself.

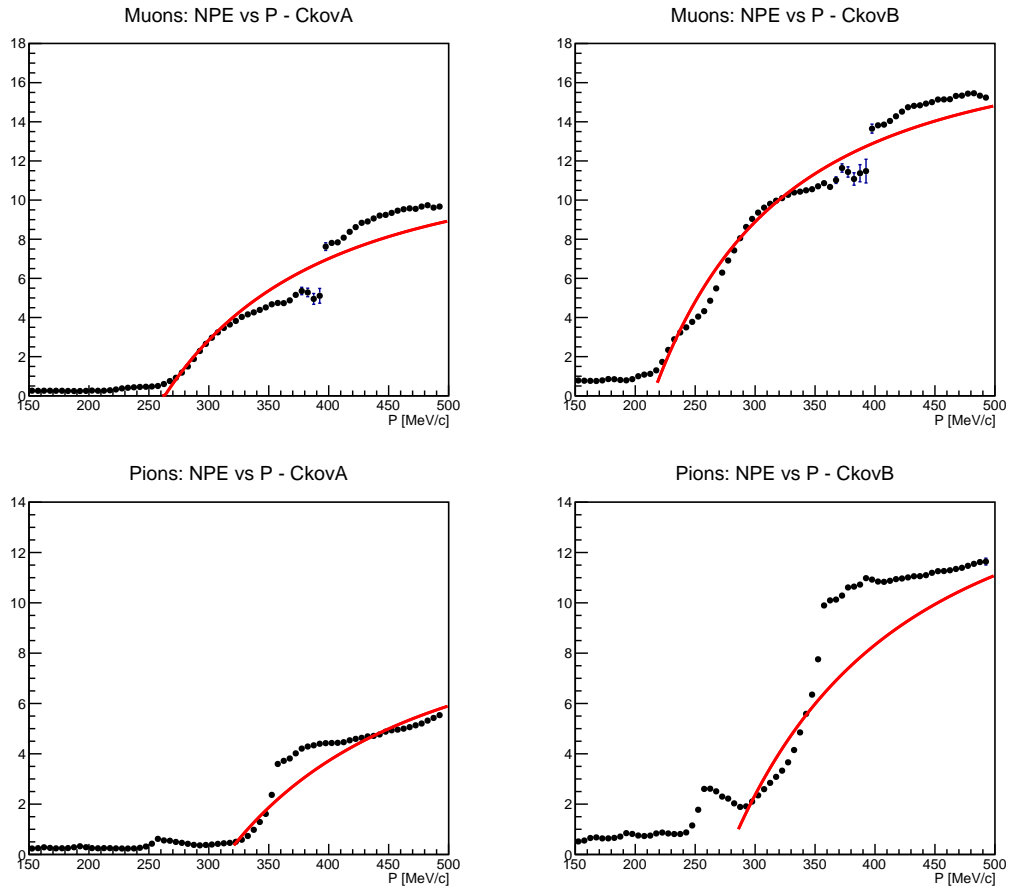


Figure 12: Photoelectron yields versus momentum for muons and pions in CkovA and CkovB with the superimposed fitted activation functions.

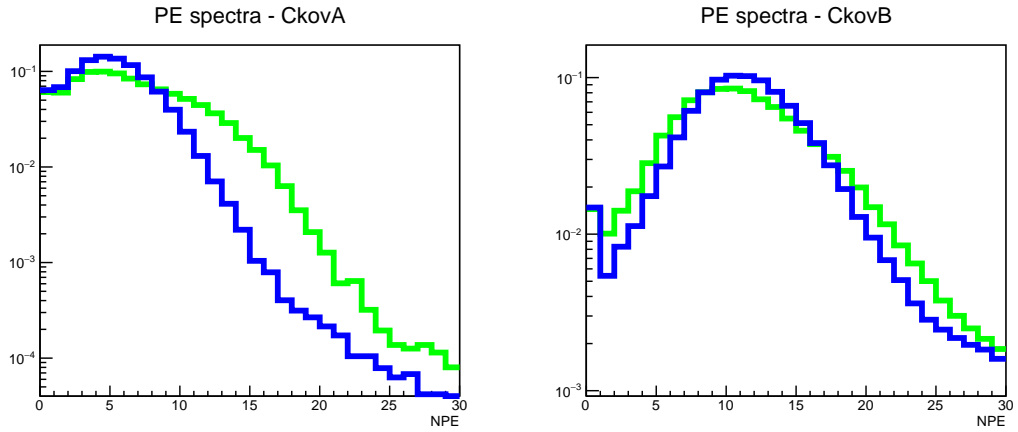


Figure 13: Photoelectron spectra in CkovA (left) and CkovB (right) for muons (green) and pions (blue) above the threshold. The distributions are both normalised.

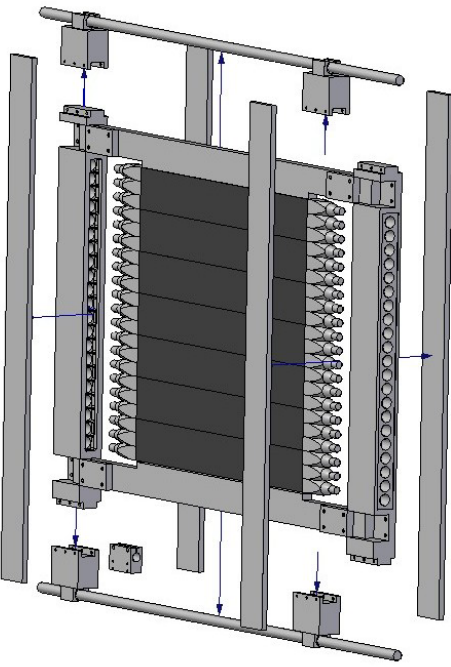


Figure 14: Magnetic shielding of KLOE-Light PMTs.

4 KLOE-Light Calorimeter

4.1 Introduction

The KLOE-Light (KL) pre-shower sampling calorimeter is composed of extruded lead foils in which scintillating fibres are placed in volume ratio scintillator:lead $\sim 2:1$, “lighter” than the one of the KLOE experiment calorimeter (1:1).

The fibres are 1 mm diameter BICRON BCF-12, scintillating in the blue, 1.35 mm distant from each other within a layer. The distance between two layers is 0.98 mm, one layer being shifted by half the fibre pitch with respect to the next. Scintillation light is guided from each slab into a total of six PMTs (three on each side). Iron shields are fitted to each photomultiplier to mitigate against large stray magnetic fields from the cooling channel (see Fig. 14). The signal from each PMT is sent to a shaping amplifier (SA) module, which shapes and stretches the signal in time in order to match the sampling rate of the flash ADCs (Fig. 15 shows the design of a single slab). A total of 7 slabs forms the whole detector, which has an active volume of $93\text{ cm} \times 93\text{ cm} \times 4\text{ cm}$.

With its 2.5 radiation lengths the KL is used to distinguish muons from decay electrons providing energy deposition and timing information and to act as pre-shower in front of the EMR. The detector has been used to estimate the level of pion contamination within the MICE muon beams to be around 1% [8].

4.2 Performance

The study of KL response to different particle types at different momenta is based on particle identification obtained by time-of-flight detector, as shown in the example of Fig. ??, by applying proper cuts on the time-of-flight spectrum. The performance is presented for 140, 170, 200, 240 and 300 MeV/c momenta at the absorber position, and depending of species population for muons, pions and electrons. The results presented below are

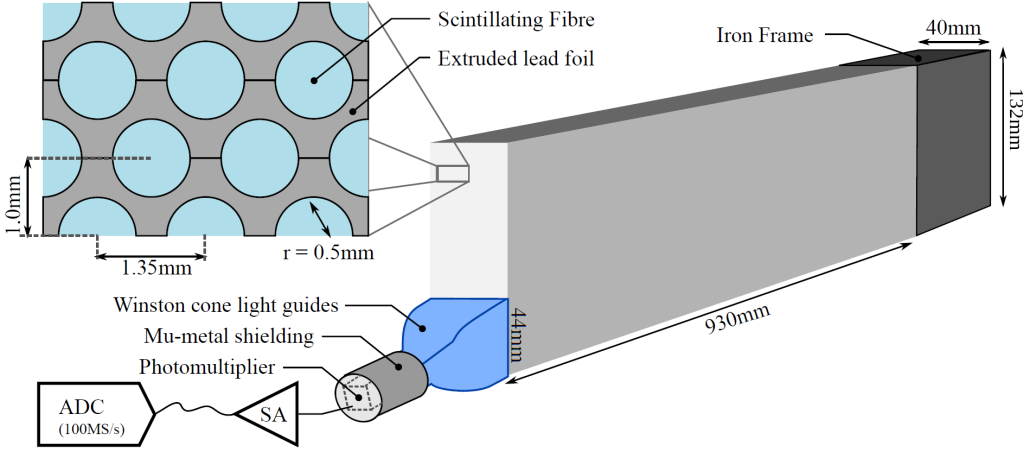


Figure 15: Single slab design of MICE KLOE-Light Calorimeter.

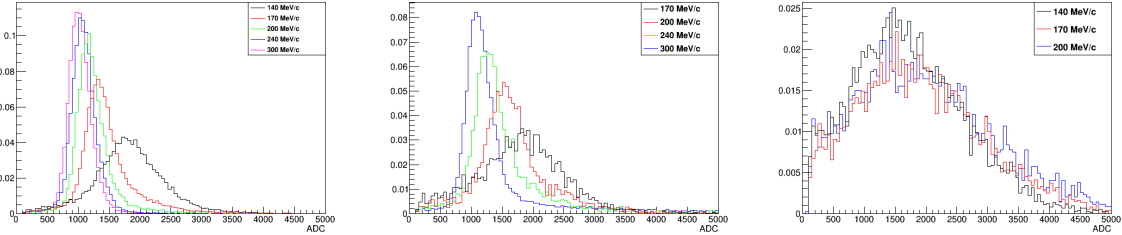


Figure 16: KL response to muons (left), pions (centre) and electrons (right) for several momenta. It is shown charge deposited by particles in KL in arbitrary units. All histograms are normalized to unity.

obtained from the straight tracks data (i.e. without magnetic fields in the trackers or focus coil) taken mainly in 2017. The KL response to muons, pions and electrons for all available momenta is presented in Fig. 16. It is clear in the cases of muons and pions that they are below mip momenta since energy deposition decreases with momentum increasing³.

For comparison of energy deposition of muon, pions and electrons for fixed momentum Fig. 17 is presented. In the case of 300 MeV/c (Fig. 17, right), where muons and pions have almost the same maximum of distribution, the tail of pions is fatter than muon one. This is due to the fact that pions experience strong interaction as well. This pion behaviour has been used to estimate its contamination in muon sample.

The number of fired KL cells by a single muon, electron or pion is given in Fig. 18 for 240 MeV/c beam. For muons we expect one, in some cases two and almost never more fired cells depending on track inclination. Pions and electrons create avalanches in KL and electron ones is much wider than the pion ones as visible of number of KL cell hits. The same figure shows number of events when if there is a reconstructed TOF track, but no signal in KL above the threshold. This can be used to calculate efficiency of KL for the three species as a function of momentum. The results are presented in Table 3 and shows that efficiency for muon registration is close to 99%.

In Fig. 19 is shown simulation of KL response to 300 MeV/c muons and pions and the distributions are

³Actually the energy deposition is defined as the sum of ADC products from all cells in KL above a given threshold. The ADC product on the other hand is the product of left and right side of one slab divided by the sum of left and right side: $ADC_{prod} = 2 \times ADC_{left} \times ADC_{right} / (ADC_{left} + ADC_{right})$. The factor 2 is present for normalization. The product of two sides compensates the effect of attenuation.

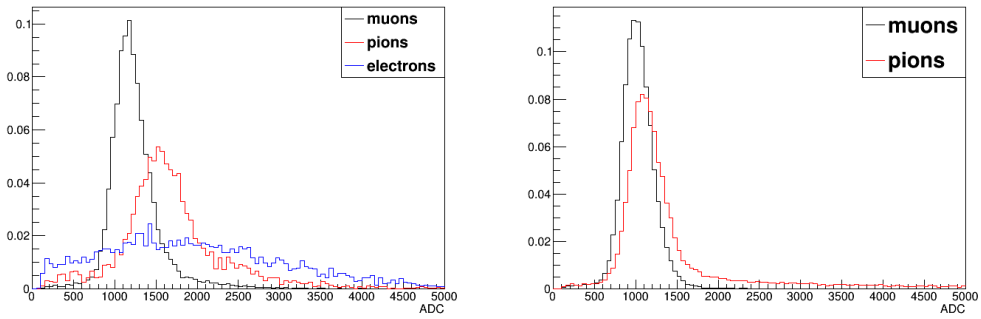


Figure 17: Comparison of energy deposition of muons, pions and electrons at 200 MeV/c (left) and of muons to pions at 300 MeV/c (right).

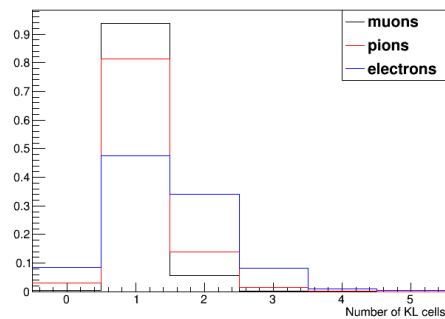


Figure 18: Particle multiplicity for 240 MeV/c, i.e. number of KL cells fired.

species	140 MeV/c	170 MeV/c	200 MeV/c	240 MeV/c	300 MeV/c
electrons	0.95 ± 0.02	0.95 ± 0.01	0.94 ± 0.03	n/a	n/a
muons	0.97 ± 0.02	0.99 ± 0.01	0.99 ± 0.01	0.99 ± 0.01	0.99 ± 0.01
pions	n/a	0.89 ± 0.03	0.95 ± 0.03	0.97 ± 0.03	0.98 ± 0.01

Table 3: Efficiency of KL for electrons, muons and pions as a function of particle momentum. The conditions required are existing of a TOF track and signal in KL above the threshold. The uncertainties are statistical.

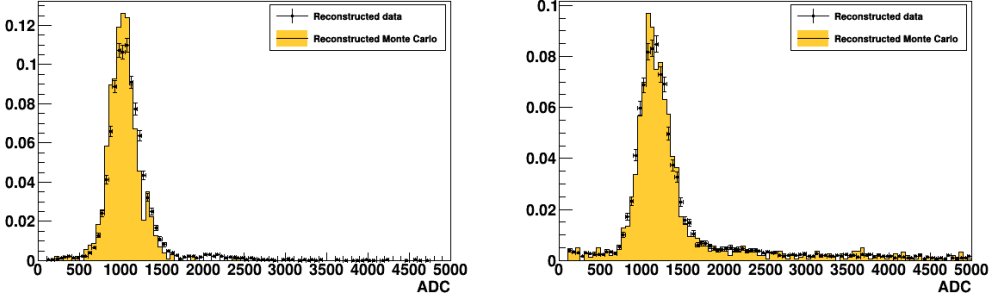


Figure 19: Comparison between data and Monte Carlo simulation of KL response to muons (left) and pions (right) at 300 MeV/c.

280 compared with data. The agreement between data and simulation is very good. The simulation is done via following steps:

- Smearing of produced photons in scintillator fibres. They obtain Poisson statistic so such is applied. In principle one can replace it with Gaussian because the number of photons created is large enough for such an approximation.
- Photoelectrons created on photomultiplier photocathode also have Poisson statistics. It cannot be replaced here with normal distribution because the number of photoelectrons is small enough so such an approximation is illegal.
- Photomultiplier gain obtains also statistical properties but it is neither Poisson nor gauss. Nevertheless it turns out that for simplicity one can use Gaussian distribution with mean value equals to PMT gain and sigma of distribution equals to half of the gain. KL photomultipliers have gain $\sim 2 \times 10^6$, so their sigma is simply 10^6 .

5 Electron Muon Ranger

5.1 Introduction

295 The Electron-Muon Ranger (EMR) is a fully-active scintillator detector [12]. It can be classified as a tracking-calorimeter as its granularity allows for track reconstruction. The EMR consists of extruded triangular scintillator bars arranged in planes. One plane contains 59 bars and covers an area of 1.27 m^2 . Each even bar is rotated by 180 degrees with respect to the odd one. A cross-section of bars and their arrangement in a plane is shown in Fig. 20. This configuration does not leave dead area in the detector for particles crossing a plane with angles that do not exceed 45 degrees with respect to the beam axis. Each plane is rotated through 90 degrees with respect to the previous one, such that a pair of planes defines a horizontal and vertical (x, y) interaction

coordinate. The light, produced when a particle crosses a bar, is collected by a wave-length shifting (WLS) fibre glued inside the bar. At both ends, the WLS fibre is coupled to clear fibres that transport the light to a photomultiplier tube (PMT). Signals produced in a plane are read out collectively on one end by a single-anode PMT for an integrated charge measurement and separately on the other by a multi-anode PMTs for individual bar hit reconstruction. The full detector is composed of 24 X-Y modules for a total active volume of $\sim 1 \text{ m}^3$.

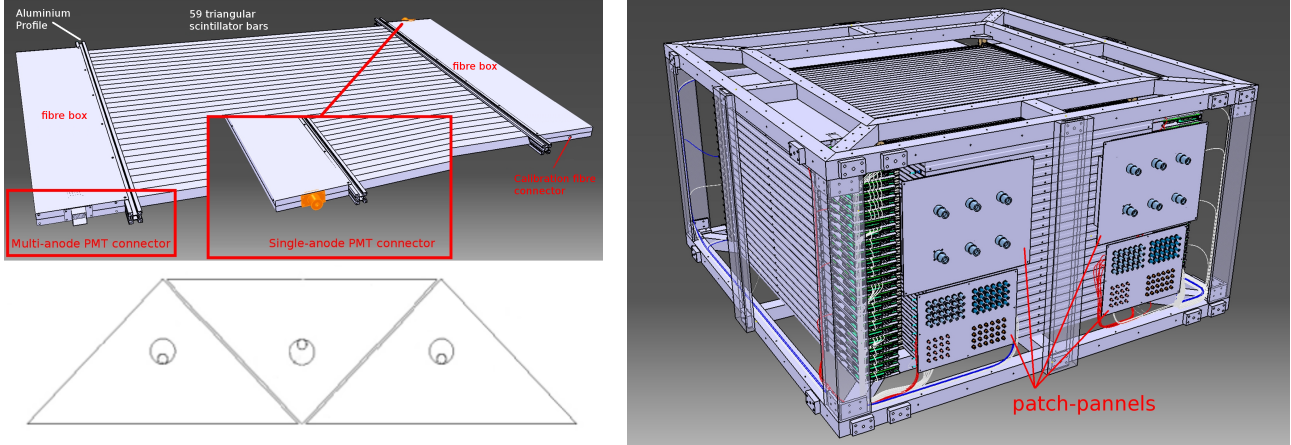


Figure 20: Drawing of one EMR plane (top left), cross section of 3 bars and their wavelength shifting fibres (bottom left) and drawing of the full detector and its supporting structure (right).

An array of analyses were conducted to characterize the hardware of the EMR and determine whether the detector performs to specifications [13]. The clear fibres coming from the bars were shown to transmit the desired amount of light, and only four dead channels were identified in the electronics. Two channels had indubitably been mismatched during assembly and the DAQ channel map was subsequently corrected. The level of crosstalk is within acceptable values for the type of multi-anode photomultiplier used with an average of $0.20 \pm 0.03\%$ probability of occurrence in adjacent channels and a mean amplitude equivalent to $4.5 \pm 0.1\%$ of the primary signal intensity. The efficiency of the signal acquisition, defined as the probability of recording a signal in a plane when a particle goes through it in beam conditions, reached $99.73 \pm 0.02\%$.

The primary purpose of the EMR is to distinguish between muons and their decay products, identifying muons that have crossed the entire cooling channel. Muons and electrons exhibit distinct behaviours in the detector. A muon follows a single straight track before either stopping or exiting the scintillating volume, while electrons shower in the lead of the KL and create a broad cascade of secondary particles. Two main geometric variables, the plane density and the shower spread, are used to differentiate them. The detector is capable of identifying electrons with an efficiency of 98.6 %, providing a purity for the MICE beam that exceeds 99.8 %. The EMR also proved to be a powerful tool for the reconstruction of muon momenta in the range 100–280 MeV/c [14].

5.2 Performance

The performance of the EMR detector is assessed at three levels of resolution with the data acquired during the 2017/02 and 2017/03 ISIS user cycles. The performance of the hardware itself is evaluated by analysing the characteristics of raw photomultiplier signals. The reconstruction efficiency is assessed by looking at higher level quantities. The performance of the detector as an electron tagging device is measured.

5.2.1 Hardware efficiencies

The data sets used to evaluate the detector hardware efficiencies are summarized in table 4. The MICE beam line is tuned to the highest attainable momentum to maximize the transmission to the EMR detector and increase the range of particles in the detector. In this configuration, the beam line produces pions and muons in comparable quantities, along with positrons. The particle species are identified by evaluating their time-of-flight between TOF1 and TOF2. The time-of-flight distribution for muons, pions and positrons is represented in figure 21. Only the particles with a time-of-flight between 28 and 28.75 ns, i.e. compatible with the muon hypothesis, are included in the analysis sample.

Run ID	Date	Type	Momentum	Spills	Triggers	EMR events
9619	19/09/2017	π^+	400 MeV/c	2289	265312	36775
9620	19/09/2017	π^+	400 MeV/c	5388	668026	107578
		Total		7677	933338	144353

Table 4: Summary of the data sets used to measure the efficiency of the EMR in the 2017/02 ISIS user cycle.

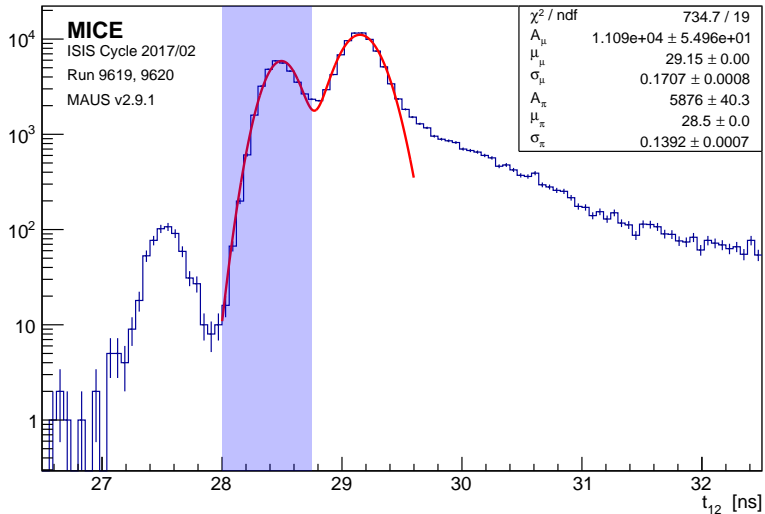


Figure 21: Time-of-flight of positrons, muons and pions for the 400 MeV/c pionic beam line used in the EMR efficiency analysis. The blue band represents the selected range.

A muon that makes it into the analysis sample has a momentum larger than 350 MeV/c right before TOF2. It is expected to cross both TOF2 and the KL without stopping and penetrate the EMR. In practice, the probability of creating an EMR event, i.e. to produce hits in the detector is $99.62 \pm 0.03\%$. The minor inefficiency may be attributed to pions in the muon sample that experience hadronic interactions in the KL. If hits are produced in the detector, space points are reconstructed $98.56 \pm 0.06\%$. This inefficiency may be associated with muon decay between TOF2 and the EMR and produce scarce hits in the detector.

To evaluate the efficiency of the scintillator planes and their readouts, only the muons which penetrate the entire detector are taken into account. If a signal is recorded in the most downstream plane, it is expected that at least a bar will be hit in each plane on its path and that a signal will be recorded in the single anode PMT. The left panel of figure 22 shows the MAPMT bar hit multiplicity for all the plane combined. It shows that in $3.26 \pm 0.02\%$ of cases, on average, a plane traversed by a muon will be not produce a signal in its MAPMT

and that the most probable amount of bars hit is one. The right panel shows the distribution of charge recorded in all the SAPMTs. A track is missed by an SAPMT $1.88 \pm 0.01\%$ of the time. This figure does not include SAPMT 26, turned off at the time of data taking.

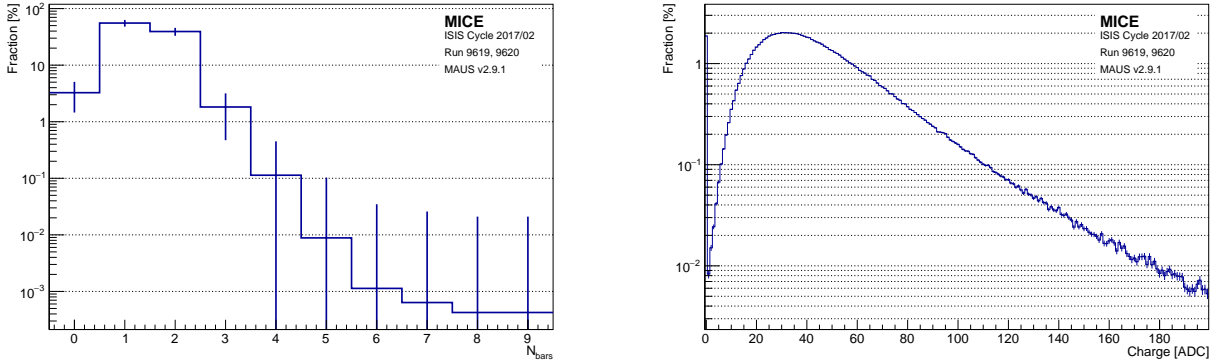


Figure 22: (Left) Global MAPMT bar multiplicity. (Right) Global SAPMT charge distribution.

Figure 23 shows the probability of recording a signal in individual MAPMTs and the SAPMTs for each of 350 the 48 planes, given a muon that crosses the whole detector. The most inefficient PMTs miss the track $\sim 10\%$ of the time. SAPMT 26 was experiencing issues during data taking and was turned off.

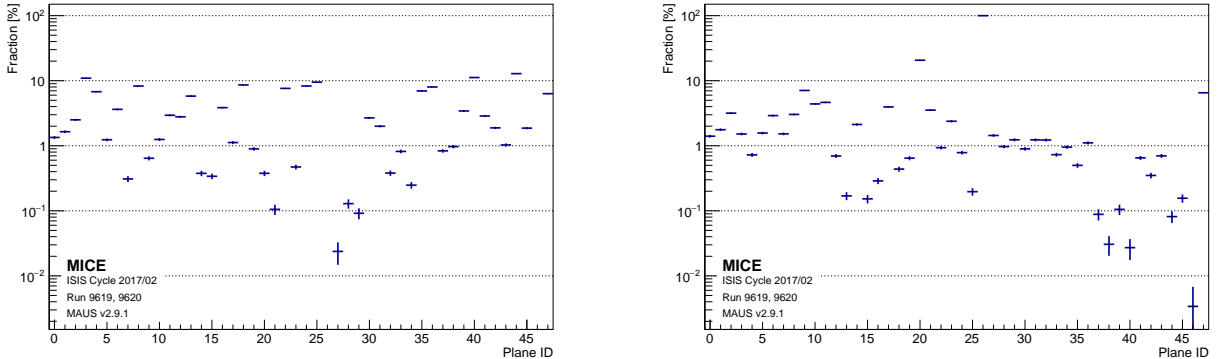


Figure 23: Probability of not producing a single bar hit in the MAPMT (left) and a zero charge in the SAPMT (right) in the 48 individual EMR planes.

5.2.2 Electron rejection

The main purpose of the Electron-Muon Ranger is to tag and reject the muons that have decayed in flight inside the experimental apparatus. A broad range of beam line momentum settings, summarized in table 5, is used 355 to characterize its muon selection efficiency. The particle species is characterized upstream of the detector by using the time-of-flight between TOF1 and TOF2. It exhibits three distinct peaks consisting of positrons, muons and pions, respectively, in order of increasing time-of-flight. The distributions of time-of-flight are shown for the data sets in range $140\text{--}240\,\text{MeV}/c$ in figure 24. The limits of the peaks are fitted to each setting in order to separate the muons and positrons into two templates upstream of the EMR. Particles that fall above the upper

360 limit of the muon peak are either pions or slow muons and are rejected from this analysis.

Run ID	Date	Type	Momentum	Spills	Triggers	EMR events
10268	26/11/2017	π^+	170 MeV/c	4418	328948	97452
10269	26/11/2017	π^+	170 MeV/c	3695	278330	82098
10262	25/11/2017	π^+	200 MeV/c	846	28103	8769
10266	25/11/2017	π^+	200 MeV/c	4365	148990	45448
10267	26/11/2017	π^+	200 MeV/c	4296	194207	53469
10275	26/11/2017	π^+	200 MeV/c	3547	126597	39114
10261	25/11/2017	π^+	240 MeV/c	4388	228337	66335
10264	25/11/2017	π^+	240 MeV/c	755	32322	10041
10265	25/11/2017	π^+	240 MeV/c	3336	134953	43129
10270	26/11/2017	π^+	240 MeV/c	222	17584	4030
10271	26/11/2017	π^+	240 MeV/c	66	5063	287
10272	26/11/2017	π^+	240 MeV/c	177	13538	1967
10273	26/11/2017	π^+	240 MeV/c	4339	232488	67350
10274	26/11/2017	π^+	240 MeV/c	738	38734	11123
Total			35188	1808194	530612	

Table 5: Summary of the data sets used to measure the efficiency of the EMR in the 2017/02 ISIS user cycle.

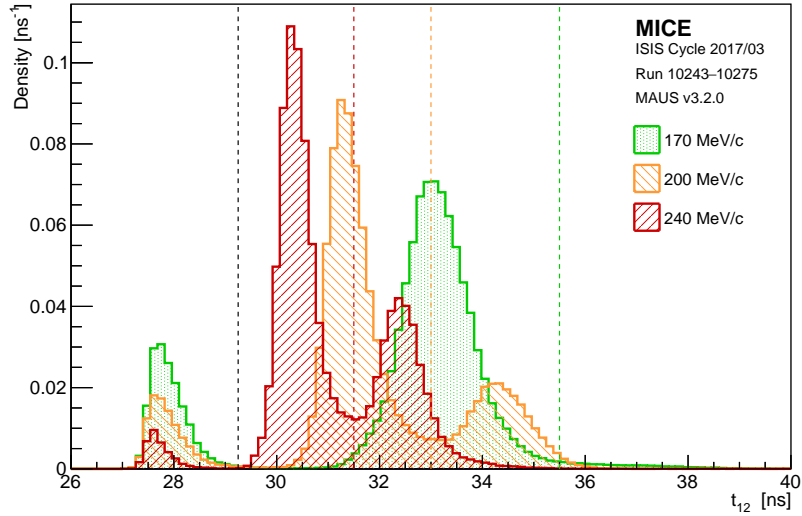


Figure 24: Time-of-flight distributions of the data sets in the range 170–240 MeV/c used in the EMR performance analysis. The dashed black line represents the upper bound of the positron peak and the coloured lines the upper bounds of the muon peaks in each setting.

MICE is a single-particle experiment, i.e. the signals associated with a trigger originate from a single particle traversing the detector. The multi-anode readout of each detector plane provides an estimate of the position of the particle track in the xz or the yz projection, depending on the orientation of the scintillator bars. Figure 25 shows event displays of a muon and a positron, as observed inside the detector, in the xz and yz projections for particles in the 240 MeV/c beam line setting. The muon exhibits a clean straight track while the positron showers inside the lead of the KL and produces a disjointed and widespread signature. The particle identification

365

variables used in the EMR are based on these distinct characteristics.

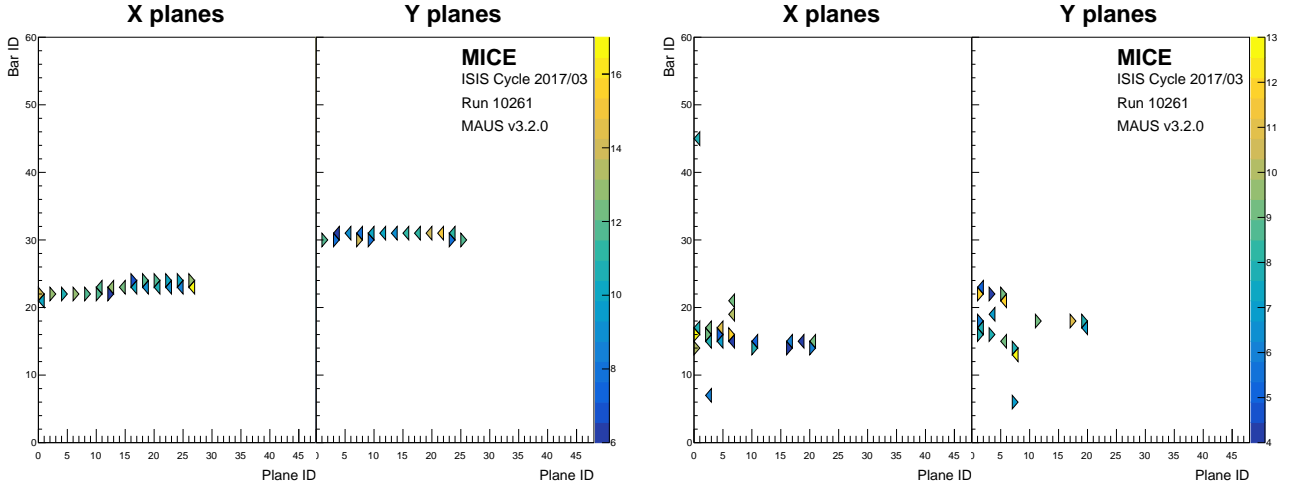


Figure 25: Event display of a muon (left) and a positron (right) from the 240 MeV/ c beam line setting, in the xz and yz projections. The colour scale represents the time-over-threshold recorded in each channel, a digitized measurement of the energy deposition in the corresponding scintillator bar.

The first particle identification statistic is the plane density, ρ_p , defined as

$$\rho_p = \frac{N_p}{Z_p + 1}, \quad (5)$$

with N_p the number of planes hit and Z_p the number of the most downstream plane. A muon deposits energy in every plane it crosses until it stops, producing a plane density close or equal to one. A positron shower contains photons that may produce hits deep inside the fiducial volume without leaving a trace on their path, reducing the plane density. The left panel of figure 26 shows the distribution of plane density of the muon and positron templates. The two templates occupy significantly different regions of plane density, as expected.

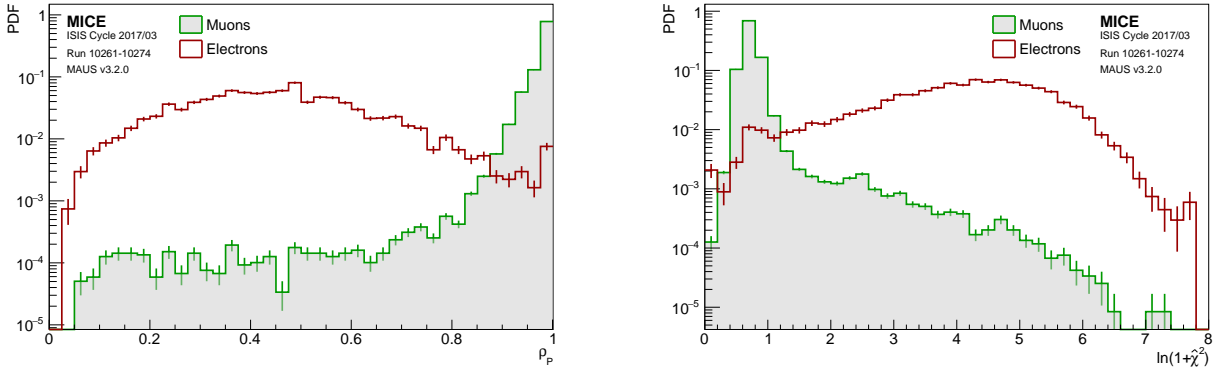


Figure 26: Plane density distribution, ρ_p (left), and normalised chi squared distribution, $\hat{\chi}^2$ (right), of the muon and electron templates in the Electron-Muon Ranger.

The second variable is the normalised chi squared, $\hat{\chi}^2$, of the fitted straight track, i.e.

$$\hat{\chi}^2 = \frac{1}{N-4} \sum_{i=1}^N \frac{\text{res}_{x,i}^2 + \text{res}_{y,i}^2}{\sigma_x^2 + \sigma_y^2}, \quad (6)$$

with N the number of space points (one per bar hit), $\text{res}_{q,i}$ the residual of the space point with respect to the track in the qz projection and σ_q the uncertainty on the space point in the qz projection, $q = x, y$ [15]. The number of degrees of freedom is $N - 4$, as a three-dimensional straight track admits four parameters. This quantity represents the transversal spread of the particle's signature. A muon follows a single track and is expected to have a $\hat{\chi}^2$ close to one, while an electron shower is expected to produce a larger value. The right panel of figure 26 shows the distribution of normalised chi squared of the muon and positron templates. The two templates occupy different regions of $\hat{\chi}^2$ but overlap more than in the case of the plane density.

The two discriminating variables are combined to form a statistical test on the particle hypothesis. Given an unknown particle species, consider a set of cuts, $(\rho_c, \hat{\chi}_c^2)$, such that

$$\begin{aligned} \rho_p > \rho_c \cap \hat{\chi}^2 < \hat{\chi}_c^2 &\rightarrow \mu^+; \\ \rho_p < \rho_c \cup \hat{\chi}^2 > \hat{\chi}_c^2 &\rightarrow e^+. \end{aligned} \quad (7)$$

Dense and narrow events will be tagged as muons while non-continuous and wide electron showers will not.

The quality of a test statistic may be characterized in terms of the loss, α , the fraction the muon sample that is rejected, and the contamination, β , the fraction of the electron sample that is selected. A test is optimal when the cost function, $\Delta = \sqrt{\alpha^2 + \beta^2}$, is minimized. Figure 27 shows the result of a scan over the parameter space. The left panel represents the cost, Δ , as a function of the two parameters that define the test statistic. Each marker in the right panel represents the value of α and β for the test values. The optimum choice of cuts yields a muon loss of 1.027 % and an electron contamination of 0.934 %.

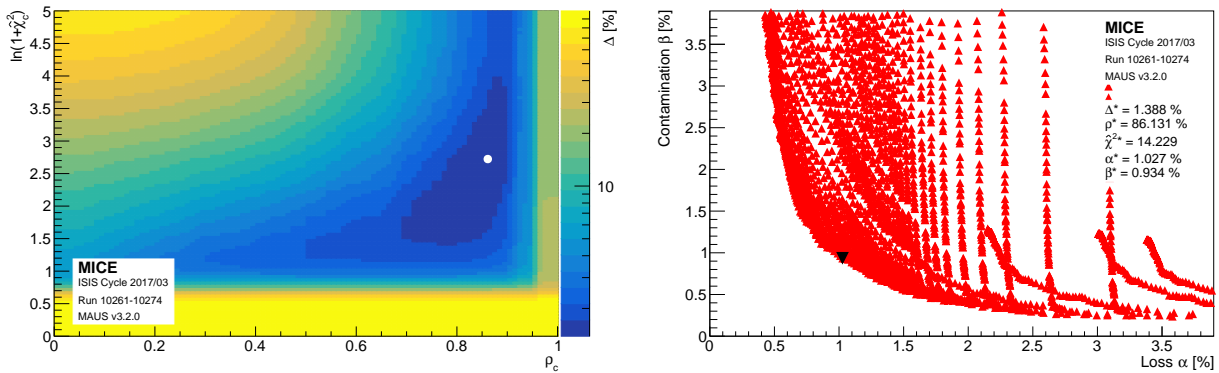


Figure 27: (Left) Cost function, $\Delta = \sqrt{\alpha^2 + \beta^2}$, as a function of the choice of cuts on the plane density and shower spread, $(\rho_c, \hat{\chi}_c^2)$. The white circle represents the minimum. (Right) Percentage of the electron sample tagged as muons (β) as a function of the loss of real muons (α).

The downstream tracker (TKD) allows for the reconstruction of each particle momentum before entering the EMR. To assess the influence of momentum on contamination and loss, their values are calculated for 10 MeV/c bins in the range 100–300 MeV/c. The test statistic performed in each bin is based on the optimal set of cuts optimized for the whole sample, i.e. $\rho^* = 86.131\%$ and $\hat{\chi}^2* = 14.229$. Figure 28 shows the loss, α , and the contamination, β , as a function the TKD momentum. It shows that, at low momentum, the apparent muon loss increases. This is due to an increase in decay probability between TOF2 and the EMR and an decrease in the amount of muons that cross the KL to reach the EMR.

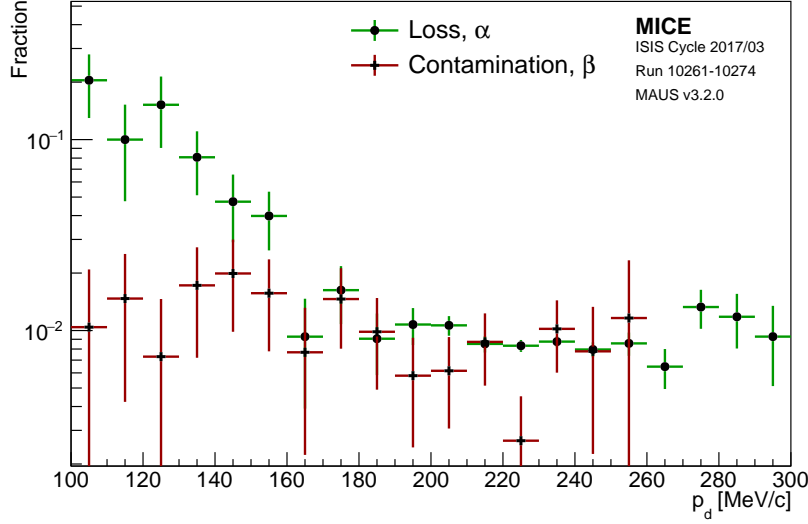


Figure 28: Percentage of electron contamination, β , and muon loss, α , for different ranges of momentum measured in the downstream tracker, p_d . The error bars are based on the statistical uncertainty in a bin.

5.2.3 Muon track momentum

The tracking capabilities of the detector enable the reconstruction of several muon parameters. Muons follow a straight track in the scintillating volume, continuously losing energy through ionization until they stop. The reconstructed track points are fitted with a straight line. The data summarized in table 5 is used to assess the tracking capability of the EMR. The left panel of figure 29 shows the distribution of origin track points, i.e. track positions at the entrance of the detector. The right panel shows the angular distribution of tracks, with respect to the z axis, as a function of the momentum reconstructed in the downstream tracker.

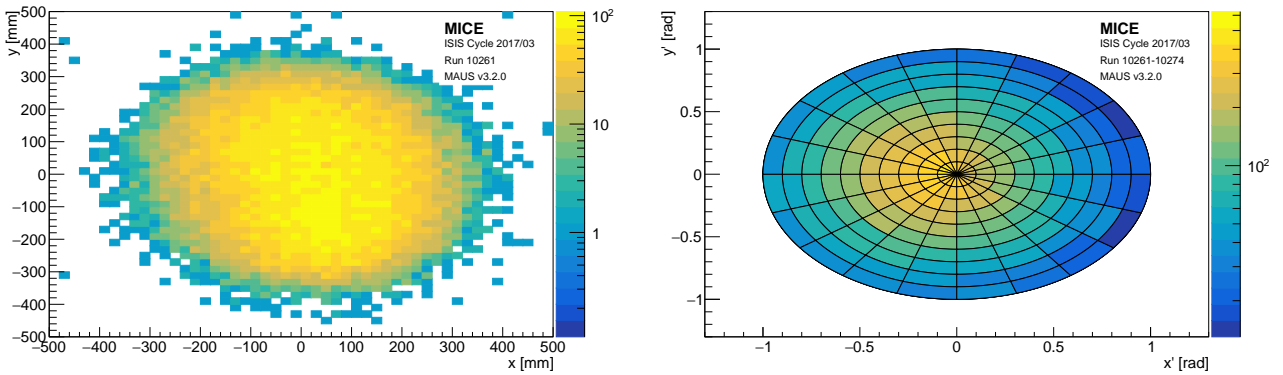


Figure 29: (Left) Beam profile at the entrance of the EMR. (Right) Polar plot of the track gradients in the EMR. The radial excursion represents the angle with respect to the z axis and the angle represents the azimuth.

The end point of a muon track is reconstructed as the final space point in the most downstream plane reached by the particle. The length of the straight track that joins the origin of the track and its end point estimates the muon range. Figure 30 shows the range of muons in the EMR for different data sets and as a function of the

momentum reconstructed from the muon time-of-flight between TOF1 and TOF2, i.e.

$$p_{12} = \frac{m_\mu c}{\sqrt{(ct_{12}/d)^2 - 1}}, \quad (8)$$

with m_μ the muon mass, t_{12} the time-of-flight and d the distance between the two TOF stations.

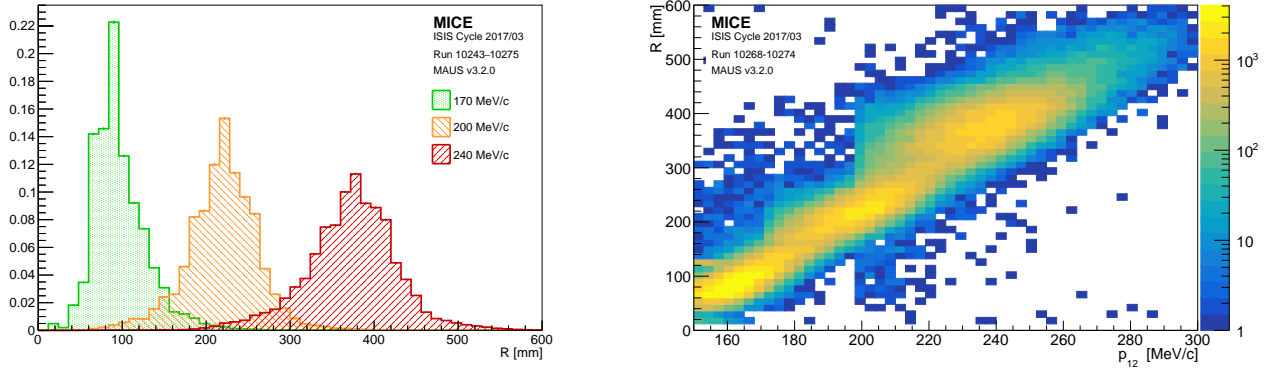


Figure 30: (Left) EMR range distributions of the data sets in the range 170–240 MeV/c. (Right) EMR range as a function of the momentum reconstructed from the time-of-flight between TOF1 and TOF2.

In the muon hypothesis, the Continuously Slowing Down Approximation (CSDA) is used to estimate the muon momentum from its range in polystyrene, the active material of the detector. The range of a muon, \mathcal{R} , in the CSDA simply reads

$$\mathcal{R} = \int_{T_0}^0 \frac{dE}{|dE/dx|} = \int_{p_0}^0 \frac{dp}{|dE/dx|} \beta c, \quad (9)$$

with T_0 , p_0 the kinetic energy and momentum of the impinging momentum and dE/dx the mean ionization energy loss. The impinging momentum, p_0 , may be recovered by numerically inverting equation 9. The momentum reconstructed from the time-of-flight between TOF1 and TOF2, p_{12} , is propagated to the entrance 405 of the EMR by subtracting the energy lost in TOF2 and the KL. This provides an estimate of p_0 that may be used to validate the momentum reconstruction in the EMR, as shown in figure 31.

6 The Trackers

6.1 Introduction

MICE is equipped with two identical, high precision scintillating-fibre ("sciFi") trackers, described in [1]. Each 410 tracker is placed in a superconducting solenoid designed to provide a uniform field over the tracking volume. One tracker, TKU, is upstream of the cooling cell, the other, TKD, downstream. Each tracker consists of five detector stations, labelled 1 to 5, with the stations placed varying distances apart to help resolve ambiguities. The trackers are placed symmetrically about the cooling cell, with station 1 the nearest to the cooling cell for both. Each station is formed of three planes of $350\mu m$ scintillating-fibres, orientated at 120 degrees to one 415 another. Each plane consists of two layers. The fibres in each plane butt up to each other and the two layers are offset with respect to each other by a fibre radius. A charge particle will then deposit energy in at least $350\mu m$ of scintillator, providing uniform response over the whole station face. The doublet layers are glued to a sheet of mylar and the fibres are adjacent groups of seven fibres form one read-out channel. The three

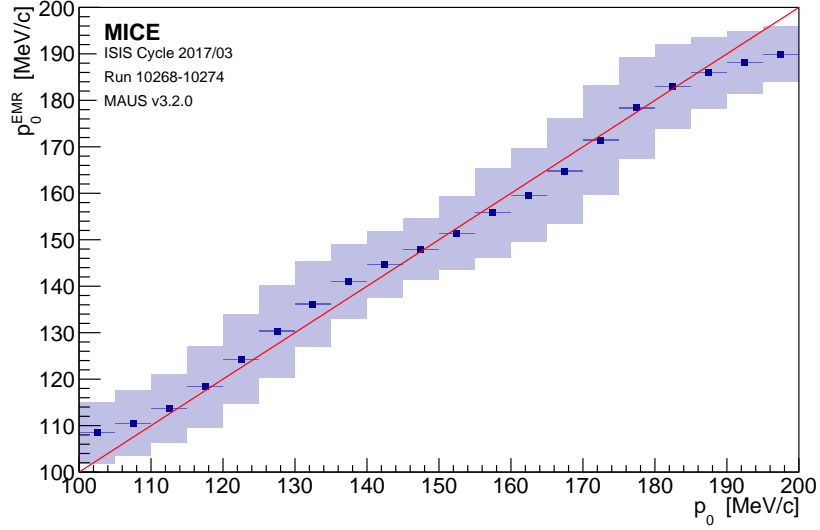


Figure 31: Momentum reconstructed in the EMR as a function of the momentum estimated at the entrance of the EMR from the time-of-flight information. The markers represent the mean in the bin, the dark band the uncertainty on the mean and the light band the RMS. The red line represents perfect agreement.

views are referred to as U, V and W, with the order being identical for each station and the U fibres running vertically. The light from the seven scintillating fibres passes into a single clear fibre, which takes it to a visible light photon counter (VLPC) which operate at 9k. The signal from the VLPCs is digitised using electronics developed by the D0 collaboration[2].

6.2 Tracker Performance and Reconstruction

6.2.1 Low Level Analysis

Low level analysis including digits, to spacepoints, 2 pages, Melissa U.

6.2.2 Noise

Noise at electronics level discussion, 1/2 page, Chris H and Noise from data, 1/2 page, Chris H

6.2.3 Track Finding Efficiency

Track selection/Kalman, efficiency (from all data runs plotted by pt and if all equal just 10mm can be shown)
resolution (from MC), reference MAUS and Tracker SW paper, 1 page, Chris H.

6.2.4 Track Fit Predicted Performance

Monte Carlo simulation used with realistic field and beam conditions in order to estimate the reconstruction performance. Run number 09964 was used, representing a typical data set used for the study of emittance

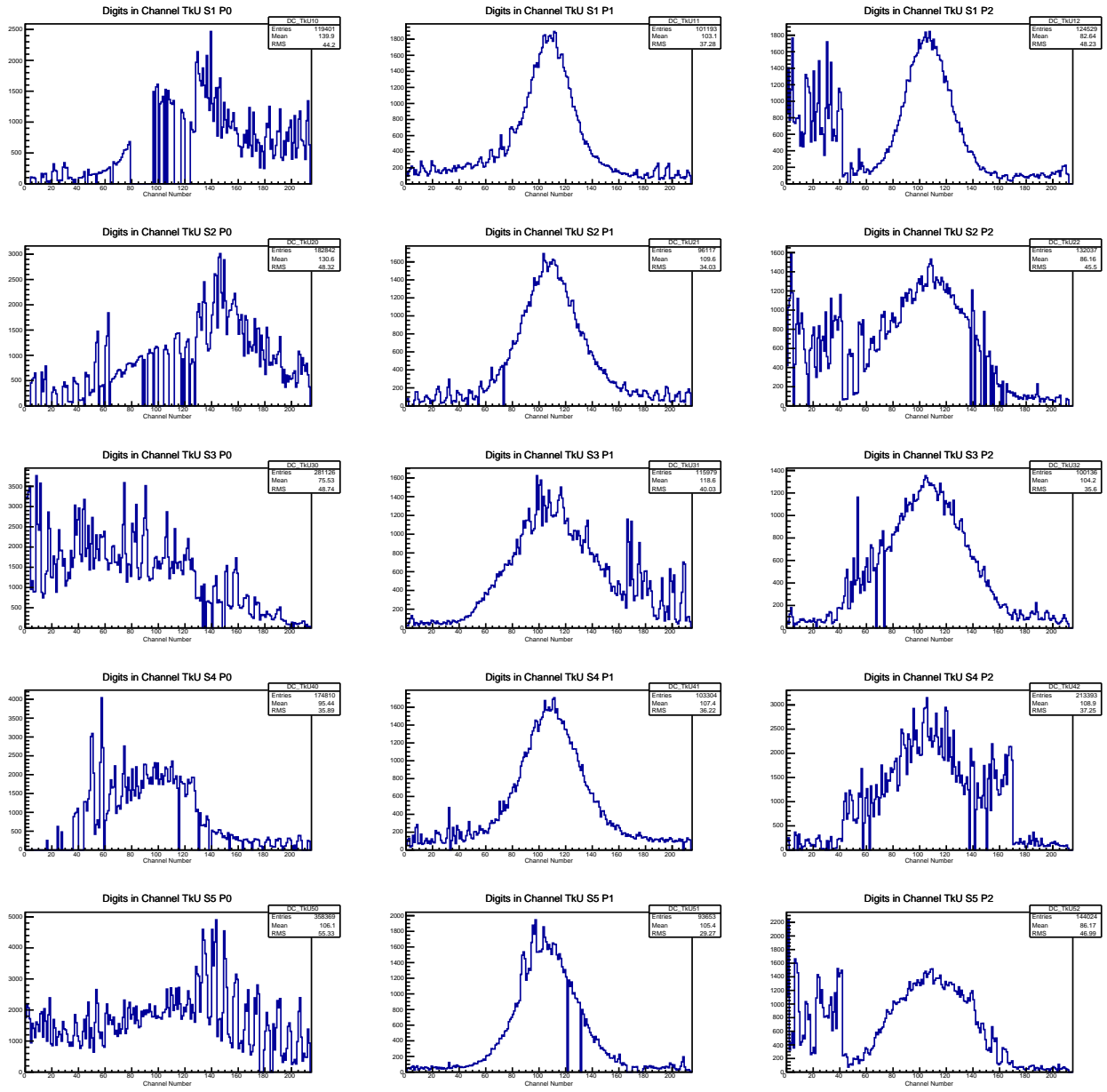


Figure 32:

evolution.

435 6.3 Tracker Efficiency Evolution

Tracker efficiency with time (maybe 1 runs every 3 months since start shown?), 1/2 page, Paul K.

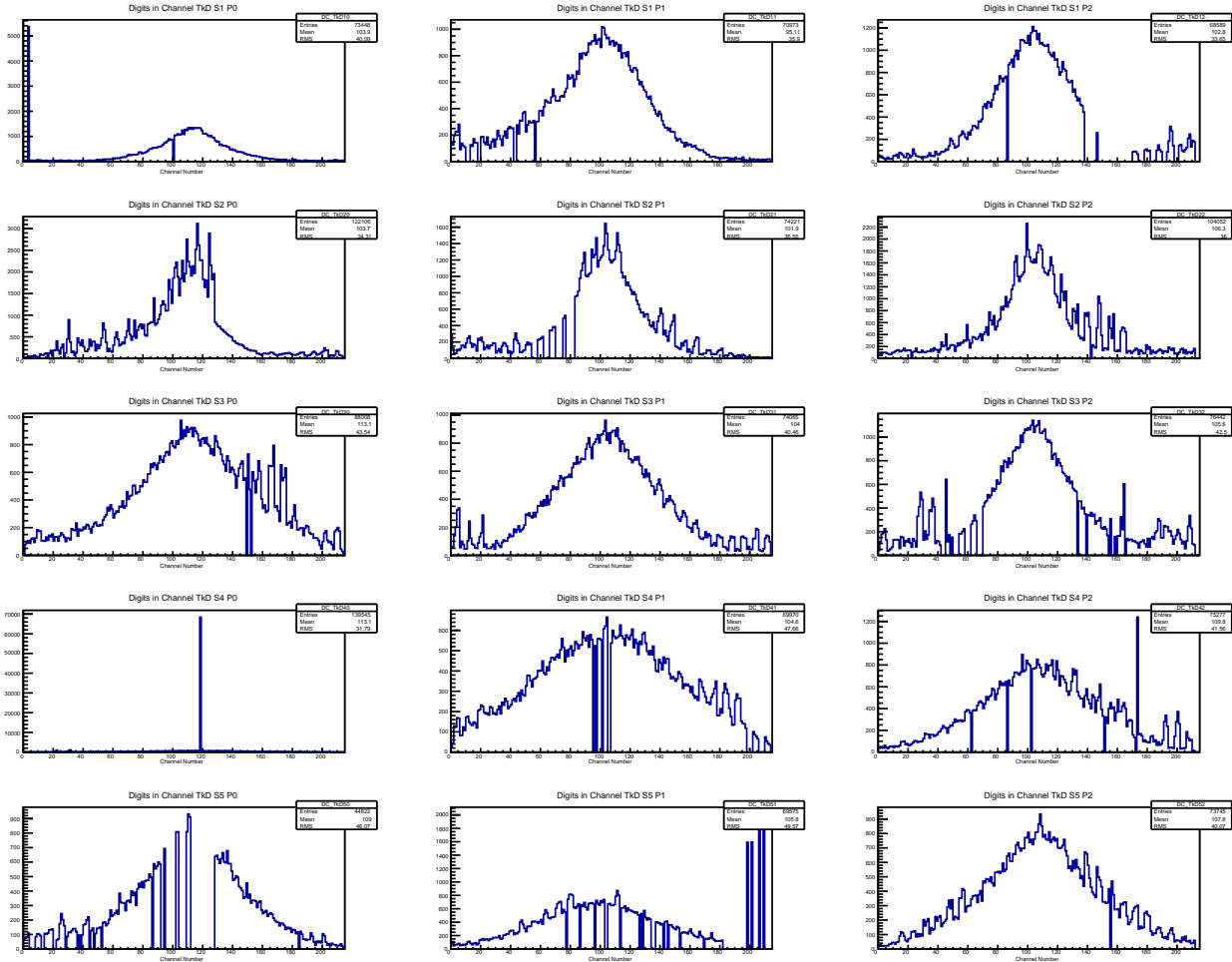


Figure 33:

7 PID

7.1 Introduction

7.2 Performance of the PID

440 8 Track Matching

8.1 Global reconstruction

The overall detector performance can be validated by extrapolating tracks from one detector to another and comparing the reconstructed coordinates with the extrapolated values. Tracks measured in the upstream tracker are extrapolated upstream to ToF1 and ToF0, and downstream to TKD and ToF2. Where there are materials in the beamline, the energy change on passing through the material is estimated using the most probable energy loss. Material thicknesses are approximated by the on-axis thickness.

Asymmetric effects can be introduced due to scattering from the walls of the cooling channel as the beam is not symmetric in the channel. In order to minimise the effects of such scattering, only events whose projected trajectory is significantly distant from the apertures are considered in this analysis. The following sample

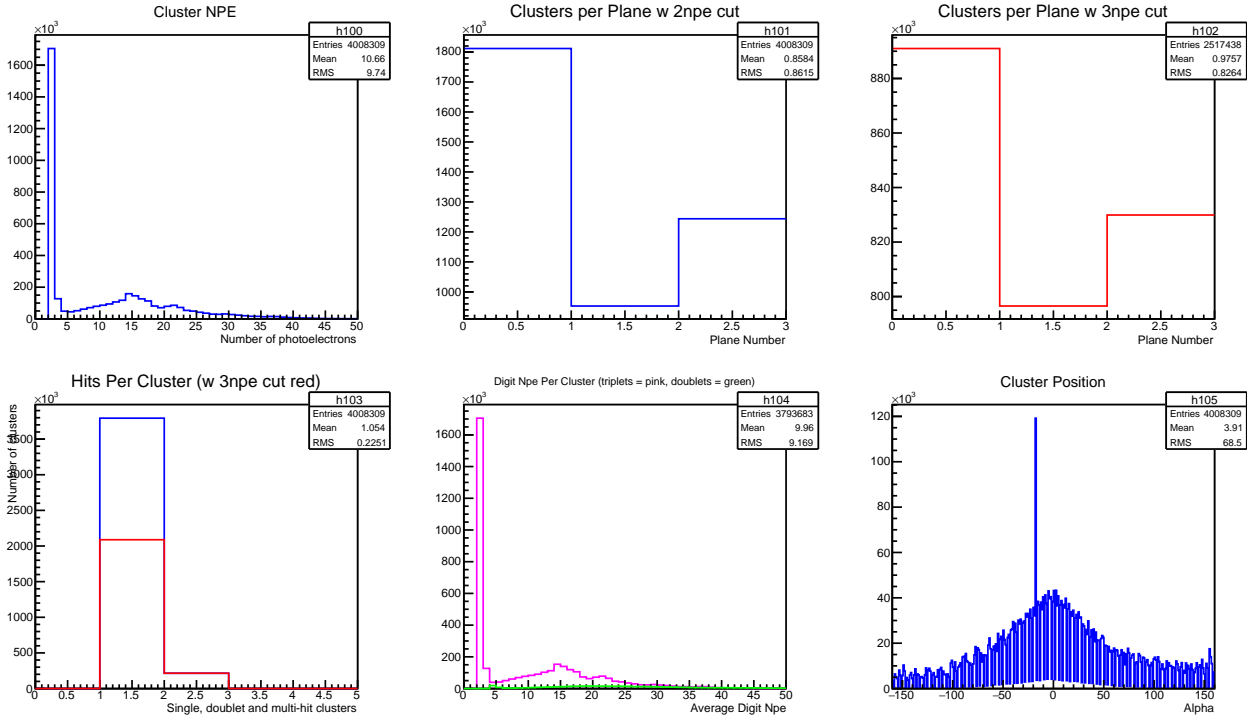


Figure 34:

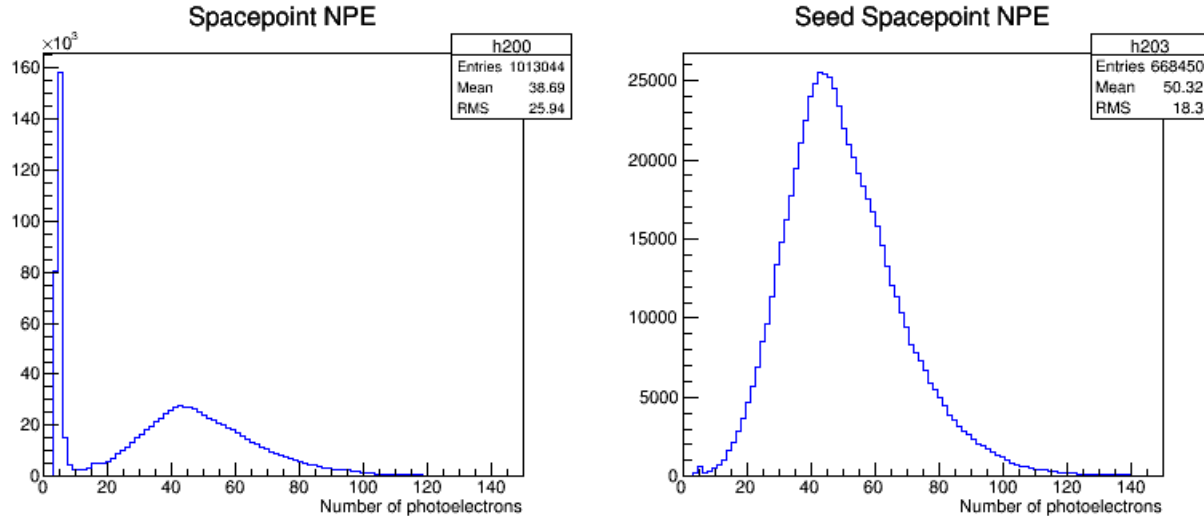


Figure 35: [left] The NPE of each spacepoint in the US and DS trackers combined. [Right] only the NPE of those spacepoints which go on to make tracks in the US and DS trackers combined are shown.

selection is considered:

- Downstream sample: Events must be included in the downstream sample to be considered in this analysis
- Aperture cut: The projected upstream track must be within 100 mm radius from the beam axis at the following apertures: the upstream absorber safety window; the upstream absorber window; the absorber centre; the downstream absorber window; the downstream absorber safety window; the upstream edge

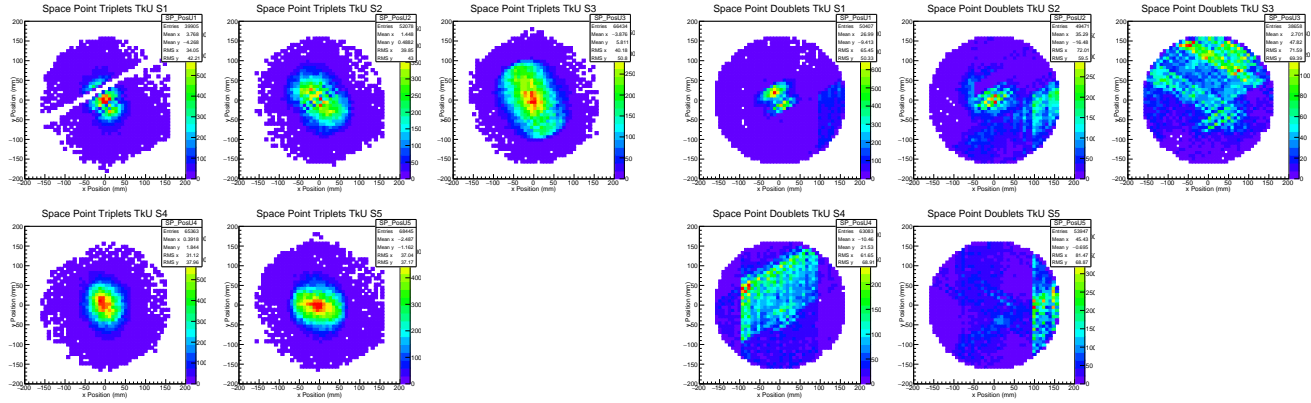


Figure 36:

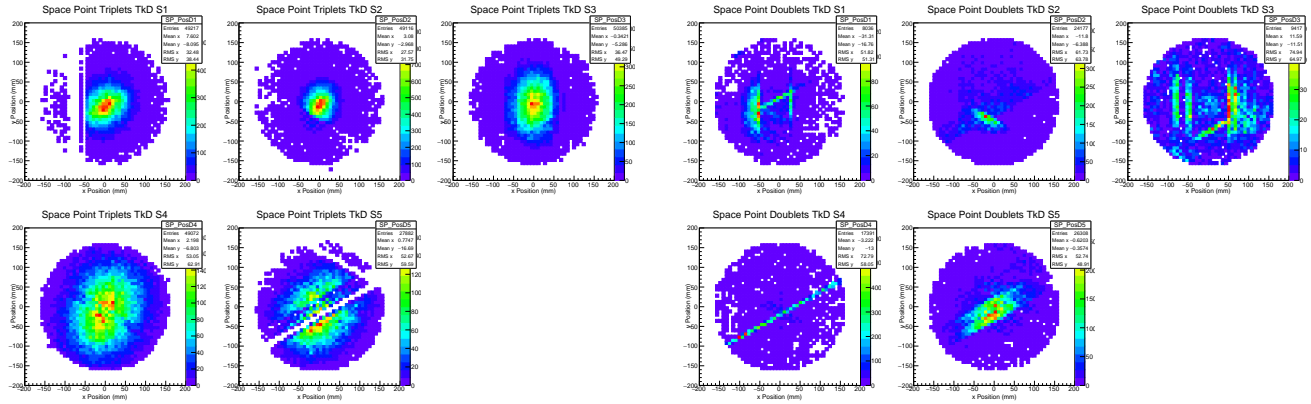


Figure 37:

455

of SSD; the Helium window in SSD; the downstream edge of the downstream PRY aperture. This is performed even when the IH2 absorber was not installed, for the sake of consistency and because in some instances mounting flanges can limit the aperture and consistency.

460

- 1 space point in ToF2: The event must have exactly one space point in ToF2.
- Successful track extrapolation to ToF2: The projected upstream track must have been successfully extrapolated to ToF2

The sample sizes are shown for data in table 6 and 7. The equivalent MC sample sizes are listed in 8 and 9.

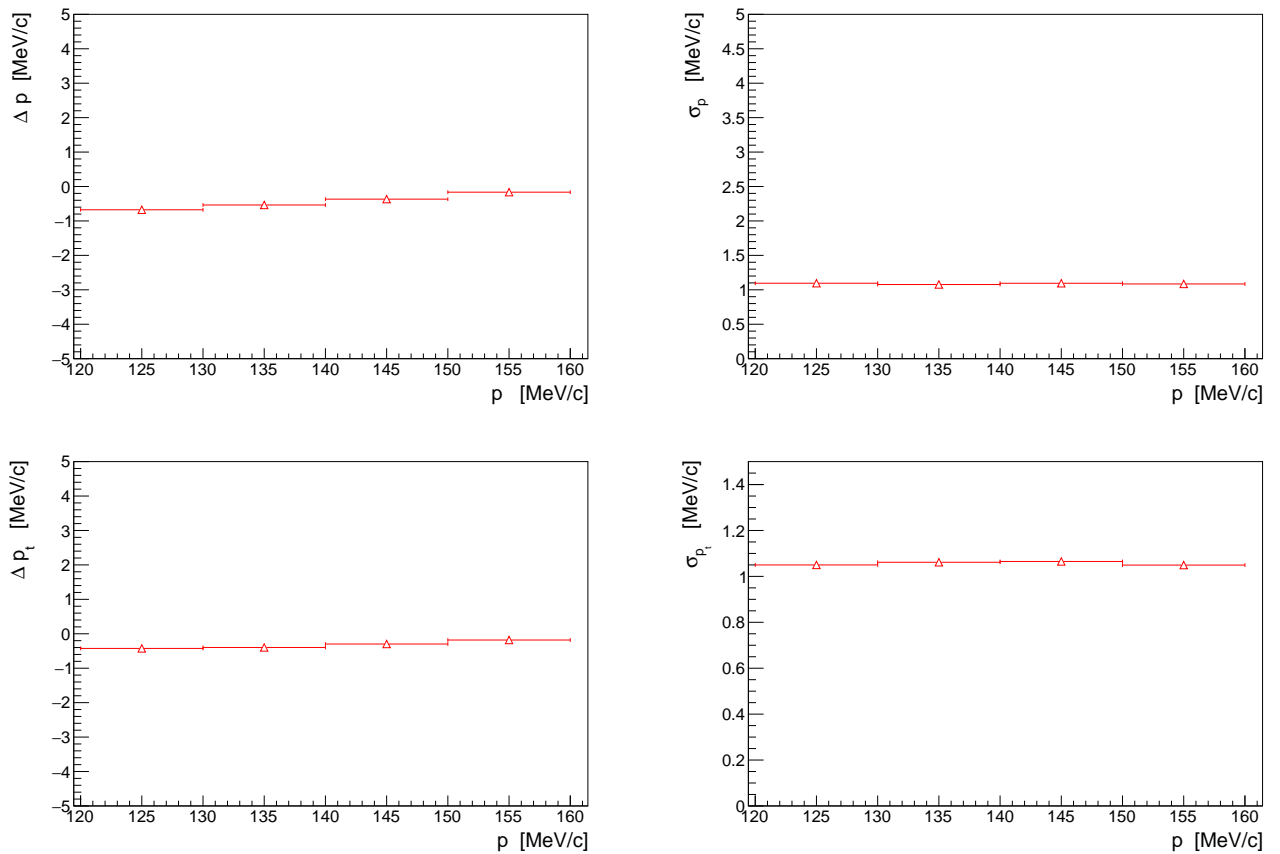


Figure 38: Predicted momentum reconstruction bias (left) and resolution (right) for the longitudinal (top) and transverse (bottom) momentum components in the upstream tracker.

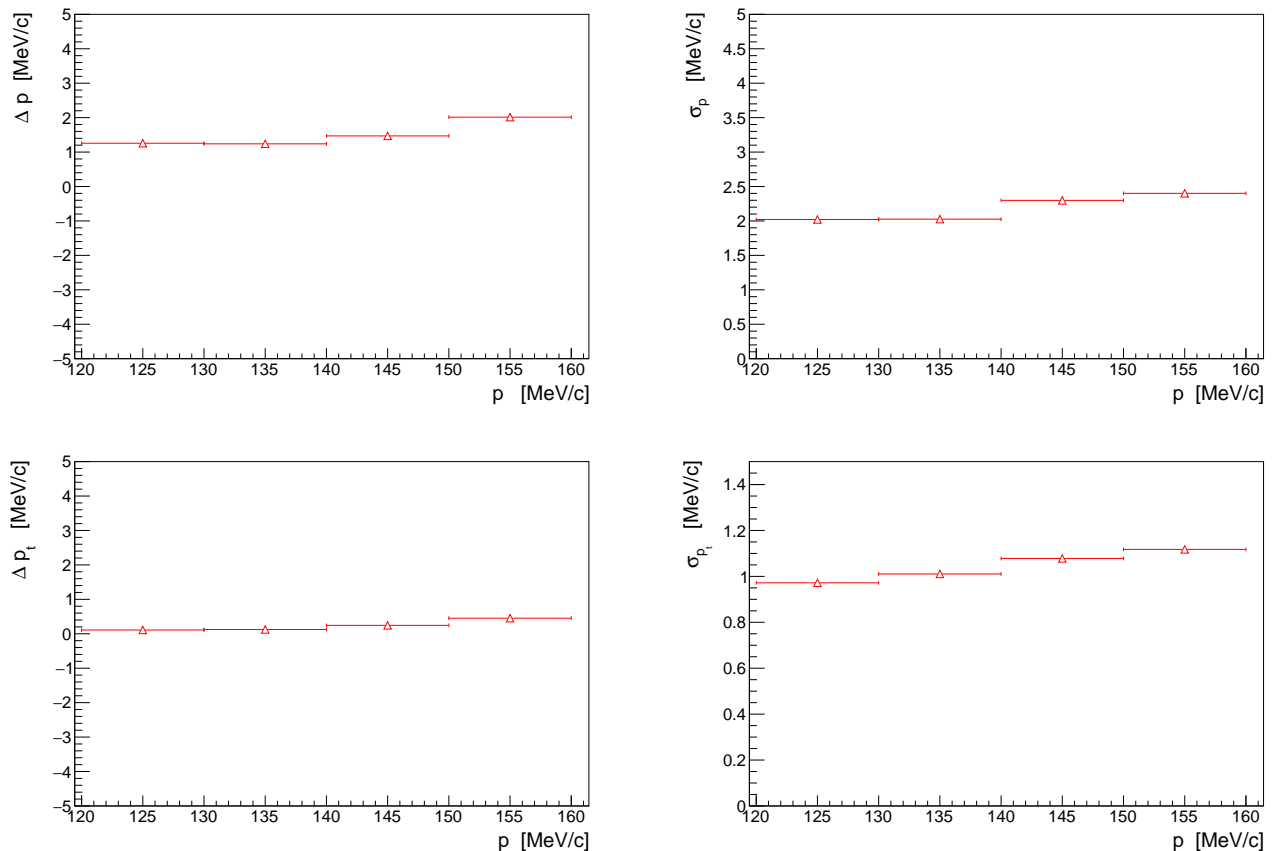


Figure 39: Predicted momentum reconstruction bias (left) and resolution (right) for the longitudinal (top) and transverse (bottom) momentum components in the downstream tracker.

Table 6: The extrapolated reconstructed data sample is listed. Samples are listed for 3-140 and 4-140 datasets.

	2017-2.7 3-140 None	2017-2.7 3-140 IH2 empty	2017-2.7 3-140 IH2 full	2017-2.7 3-140 LiH	2017-2.7 4-140 None	2017-2.7 4-140 IH2 empty	2017-2.7 4-140 IH2 full	2017-2.7 4-140 LiH
Downstream Sample	13019	8688	9058	11918	29712	23726	8407	240
Cooling channel aperture cut	7203	4721	5166	6836	17731	14571	4935	142
One space point in ToF2	6935	4506	4885	6477	16800	13817	4596	133
Successful extrapolation to TKD	6935	4506	4885	6477	16800	13817	4596	133
Successful extrapolation to ToF2	6935	4506	4885	6477	16800	13817	4596	133
Extrapolation Sample	6935	4506	4885	6477	16800	13817	4596	133

Table 7: The extrapolated reconstructed data sample is listed. Samples are listed for 6-140 and 10-140 datasets.

	2017-2.7 6-140 None	2017-2.7 6-140 IH2 empty	2017-2.7 6-140 IH2 full	2017-2.7 6-140 LiH	2017-2.7 10-140 None	2017-2.7 10-140 IH2 empty	2017-2.7 10-140 IH2 full	2017-2.7 10-140 LiH
Downstream Sample	27025	17783	29577	31257	14847	7278	14784	171
Cooling channel aperture cut	15238	10129	16045	17122	5633	2837	5057	60
One space point in ToF2	14432	9479	14826	15774	5276	2614	4471	53
Successful extrapolation to TKD	14432	9479	14826	15774	5276	2614	4471	53
Successful extrapolation to ToF2	14432	9479	14826	15774	5276	2614	4471	53
Extrapolation Sample	14432	9479	14826	15774	5276	2614	4471	53

Table 8: The extrapolated reconstructed simulated sample is listed. Samples are listed for 3-140 and 4-140 datasets.

	Simulated 2017-2.7 3-140 None	Simulated 2017-2.7 3-140 IH2 empty	Simulated 2017-2.7 3-140 IH2 full	Simulated 2017-2.7 3-140 LiH	Simulated 2017-2.7 4-140 None	Simulated 2017-2.7 4-140 IH2 empty	Simulated 2017-2.7 4-140 IH2 full
Downstream Sample	8585	8567	8511	8624	18247	18247	18455
Cooling channel aperture cut	5112	4715	5032	5378	10884	10997	10758
One space point in ToF2	4540	4184	4499	4820	9544	9747	9467
Successful extrapolation to TKD	4540	4184	4499	4820	9544	9747	9467
Successful extrapolation to ToF2	4540	4184	4499	4820	9544	9747	9467
Extrapolation Sample	4540	4184	4499	4820	9544	9747	9467

Table 9: The extrapolated reconstructed simulated sample is listed. Samples are listed for 6-140 and 10-140 datasets.

	Simulated 2017-2.7 6-140 None	Simulated 2017-2.7 6-140 IH2 empty	Simulated 2017-2.7 6-140 IH2 full	Simulated 2017-2.7 6-140 LiH	Simulated 2017-2.7 10-140 None	Simulated 2017-2.7 10-140 IH2 empty	Simulated 2017-2.7 10-140 IH2 full
Downstream Sample	17810	18031	18188	18259	8843	9029	9155
Cooling channel aperture cut	10289	10071	9449	9906	3424	3393	3227
One space point in ToF2	9014	8766	8219	8577	2941	2926	2772
Successful extrapolation to TKD	9014	8766	8219	8577	2941	2926	2772
Successful extrapolation to ToF2	9014	8766	8219	8577	2941	2926	2772
Extrapolation Sample	9014	8766	8219	8577	2941	2926	2772

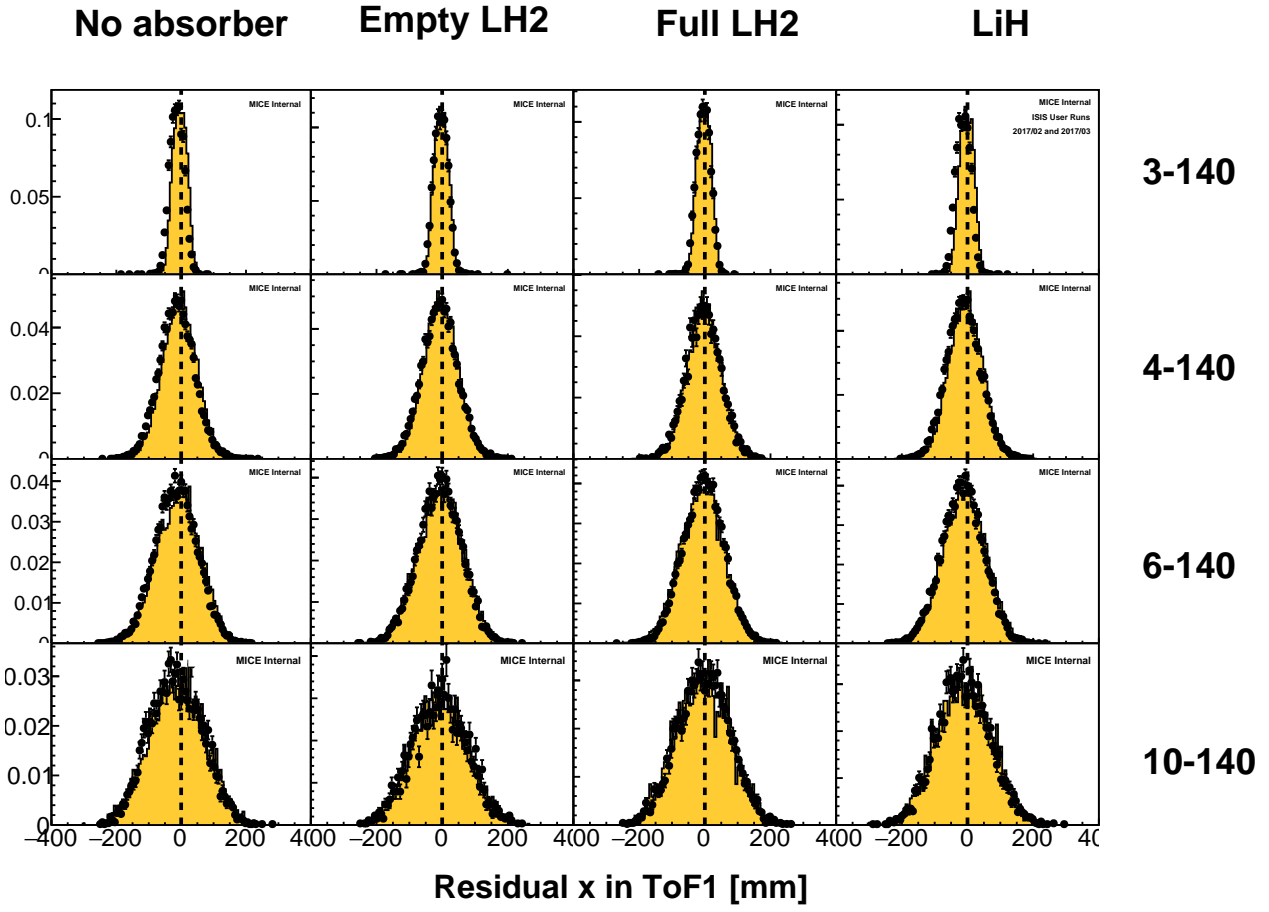


Figure 40: Residual horizontal (x) position in ToF1 of tracker tracks following extrapolation from TKU.

The extrapolated position following extrapolation to ToF1 is shown in fig. 40 and 41. In general the width of the distributions are comparable between MC and data. Where the diffuser is in place for higher emittance beams, the extrapolation goes through the diffuser material so the residuals are wider, owing to the increased scattering from the diffuser.

465

The time-of-flight residual in data shows a systematic offset from 0 and relative to the MC, as in Fig.42. The offset from 0 gets worse for higher emittance beams. It is thought to be an intrinsic property of the beam; muons that are scattered in materials between the tracker and the TOF have systematically shorter path lengths than the extrapolated trajectories, resulting in systematically longer extrapolated time of flight. The MC reconstruction is known to have issues, as evidenced by the discrepancy in slab dt for ToF0 and ToF1.

470

Plot momentum vs dt for ToF01 and ToF12

Small misalignments between TKU extrapolated tracks and TKD are observed, indicated by the offset of transverse variables from 0, shown in fig. 43 and 44. There are known, uncorrected misalignments in the detector system and there are expected to be additional misalignments in the magnets which could lead to these offsets.

475

The total momentum shows discrepancy between TKU and TKD of about 1 MeV/c. This is consistent with the systematic offset in the tracker momentum resolution shown in fig. ?? and ???. It is interesting to note that the level of agreement between MC and data varies on a setting-by-setting basis in a statistically significant manner. Agreement is better for the settings where the liquid hydrogen windows were installed.

480

Further small misalignments are observed in the position residuals between TOF2 and tracks extrapolated

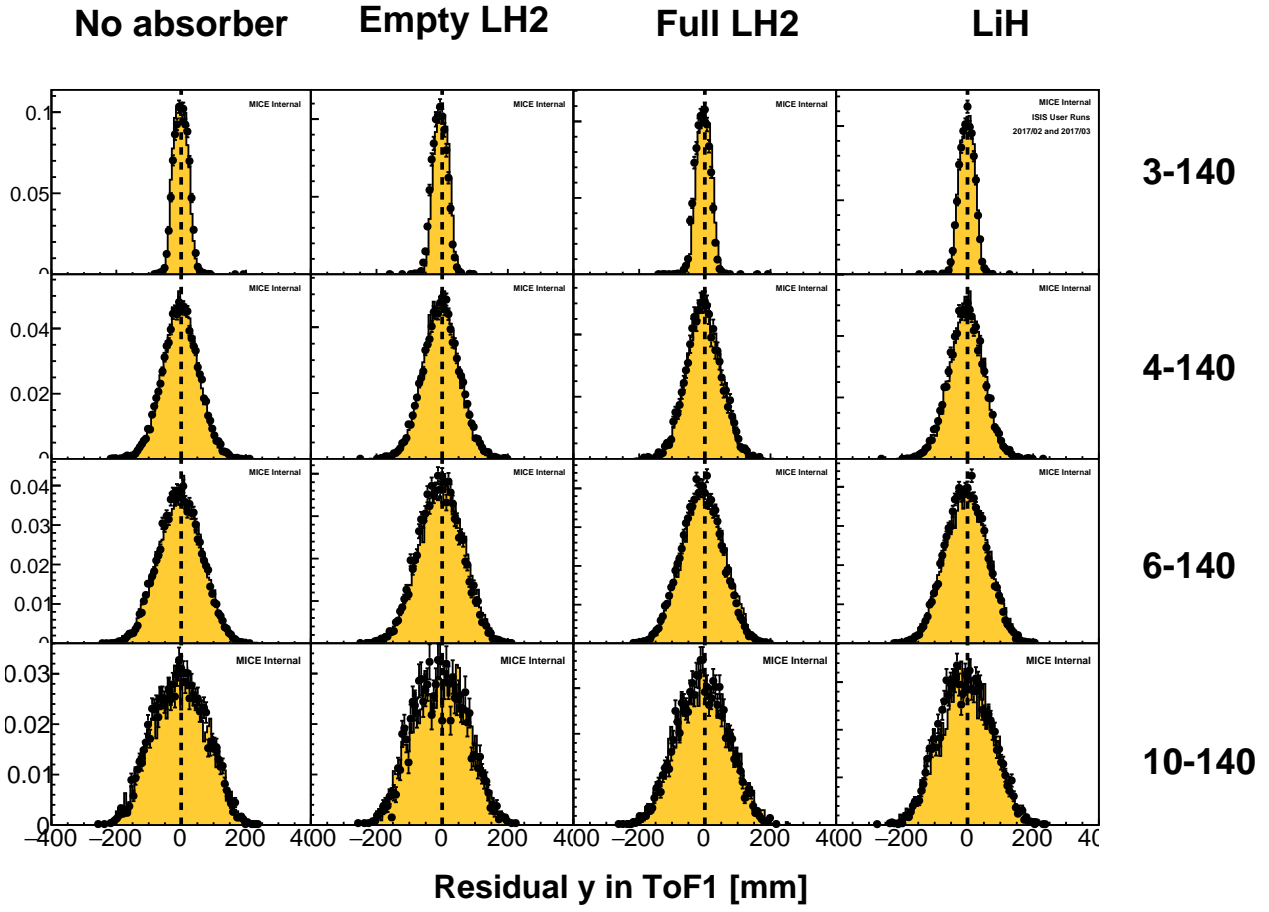


Figure 41: Residual vertical (y) position in ToF1 of tracker tracks following extrapolation from TKU.

from TKD. This is attributed to alignment issues.

TOF2 exhibits a significant offset from the extrapolated track.

8.2 Beam based magnet alignment

9 Beam-based detector alignment

485 To carry out its program, MICE requires all of its detectors to reconstruct space points in a globally consistent fashion. A beam-based alignment algorithm was developed to improve the resolution on the position of the scintillating-fibre trackers lodged inside the bores of superconducting magnets. This method can achieve unbiased measurements of the trackers rotation angles with a resolution of $6 \text{ mrad}/\sqrt{N}$ and of their position with a resolution of $20 \text{ mm}/\sqrt{N}$, with N the number of selected tracks. This section briefly describes the alignment
490 algorithm and presents the results obtained during the 2017/01 ISIS user cycle as an example case. The procedure is described in greater details and cross-checked on several simulations in [16].

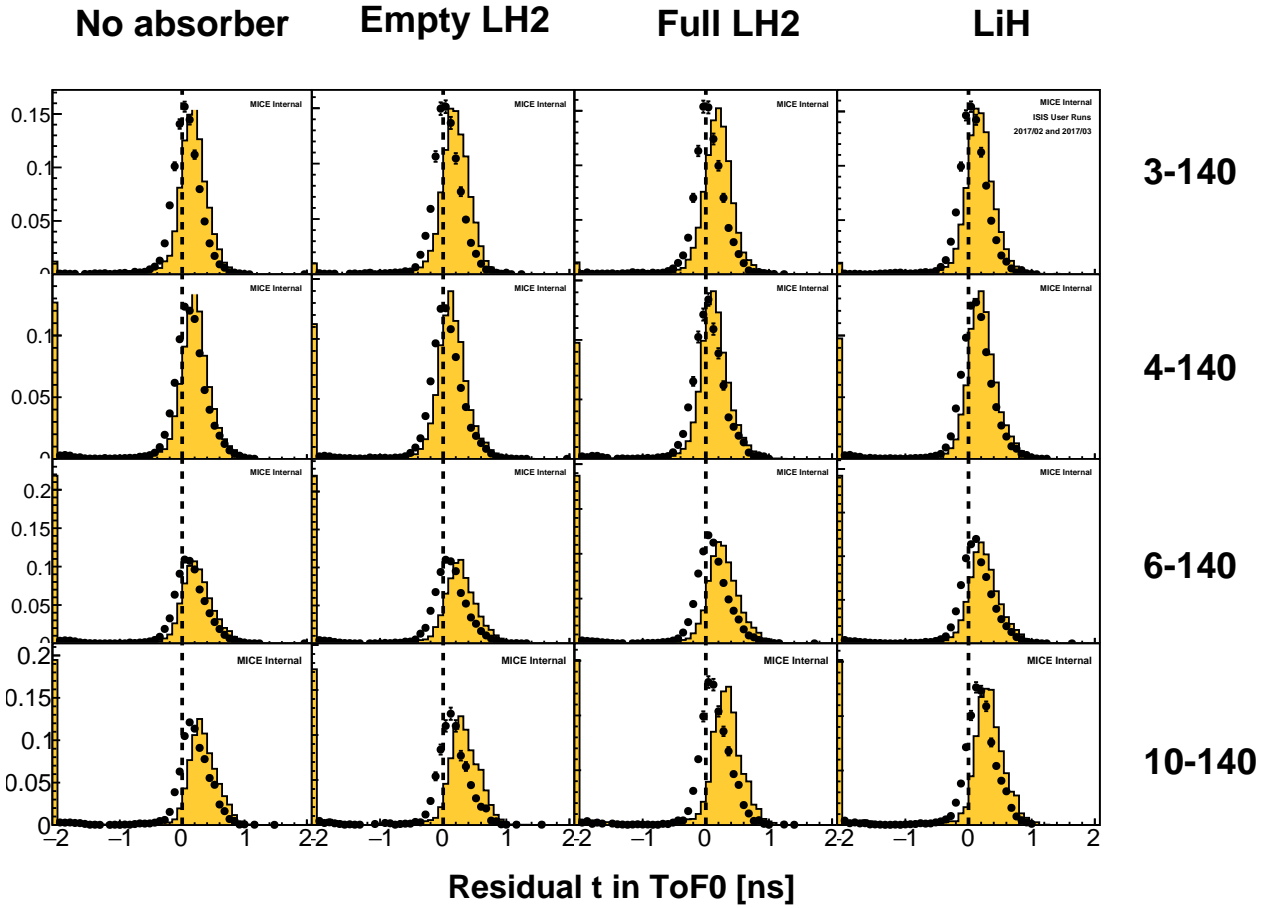


Figure 42: Residual ToF0 time of the extrapolated track. Track trajectories were drawn from TKU, while the track times were drawn from ToF1 with appropriate offsets for time-of-flight from TKU to ToF1 considered.

9.1 Introduction

The single-particle nature of the MICE experiment requires reliable global track matching throughout, i.e. the ability to associate a trace measured in the upstream tracker with one in the downstream tracker but also with the particle identification detectors. The many detectors must reconstruct space points in a globally consistent fashion to guarantee reliable and efficient track matching, as well as unbiased muon scattering measurements.

The baseline for the beam-based alignment is the surveys of the detectors in the hall using laser telemetry. Surveys were performed regularly throughout the MICE Step IV commissioning phase and data taking period. The TOF1 time-of-flight hodoscope was moved periodically to access the upstream end of the superconducting solenoids and resurveyed systematically. The downstream particle identification detectors module, composed of TOF2, the KL and the EMR, was also repositioned on occasion. The focus coil module was moved in and out of the beam line to change absorbers. Each of these events was followed by a complete resurvey.

The particle identification detectors are each equipped with at least four survey monuments and are surveyed directly. The two scintillating fibre trackers, nested in the superconducting solenoids, can not be accessed. The upstream and downstream flanges of each solenoid are surveyed and the end plate of the trackers are surveyed with respect to the flanges. The estimated position of the trackers within the bores are inferred from these measurements. A laser theodolite is used to locate the monuments with respect to the datum point situated under

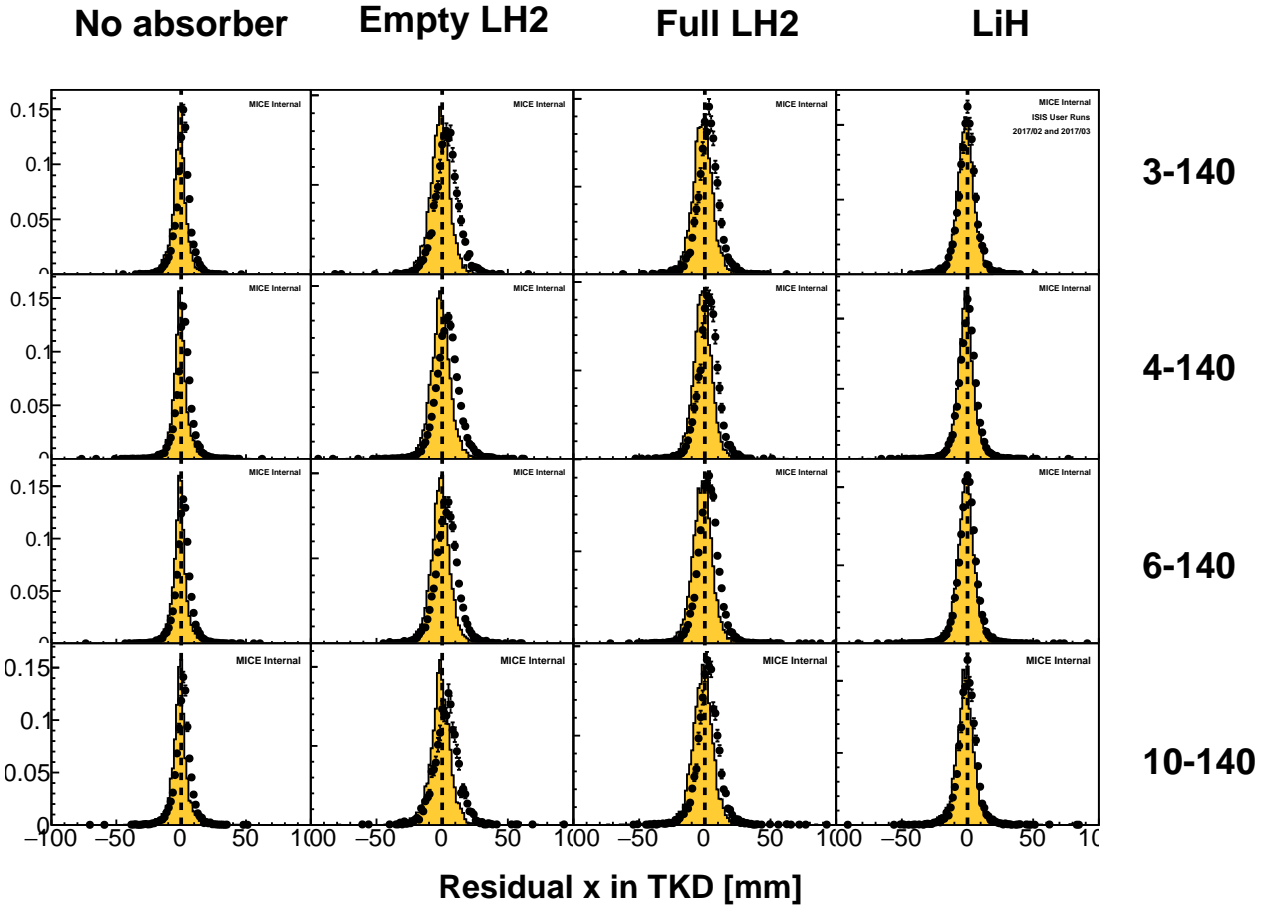


Figure 43: Residual x position of TKU tracks extrapolated to TKD, as compared to the tracks in TKD.

the second dipole magnet, D2. Figure 51 shows a picture of TOF2 and the location of its survey monuments.

Before being placed inside the magnets, each tracker was surveyed independently using a coordinate-measuring machine (CMM). This ensures that the position of the five stations is well known within each tracker with respect to the end plate. Figure 52 shows the disposition of the stations in the downstream scintillating fibre tracker and their position as measured by the CMM. The reference position is the axis that joins the centre of station 1 to the centre of station 5. The positions of stations 1 to 3 are measured with respect to that axis. The beam can be used to check the tracker station alignment.

Special care is taken during the installation of the trackers within the magnet bores. The installation platform is adjustable to enable the tracker to be aligned with the bore of the solenoid. The tracker sits on four adjustable feet, two at each end. The adjustable feet are used to align the tracker with the magnetic axis of the solenoid. Once this has been done, the location bracket is fitted. The location bracket locks the tracker in its longitudinal and azimuthal positions.

520 9.2 Analysis method

The position of tracker $t = u, d$ in global coordinates is entirely defined by the location of its centre (x_T, y_T, z_T) and a set of Tait-Bryan angles ($\alpha_T, \beta_T, \gamma_T$). The z axis is oriented along the beam line and points downstream, the y axis points upwards and the x axis completes the right-handed coordinate system. The rotation about

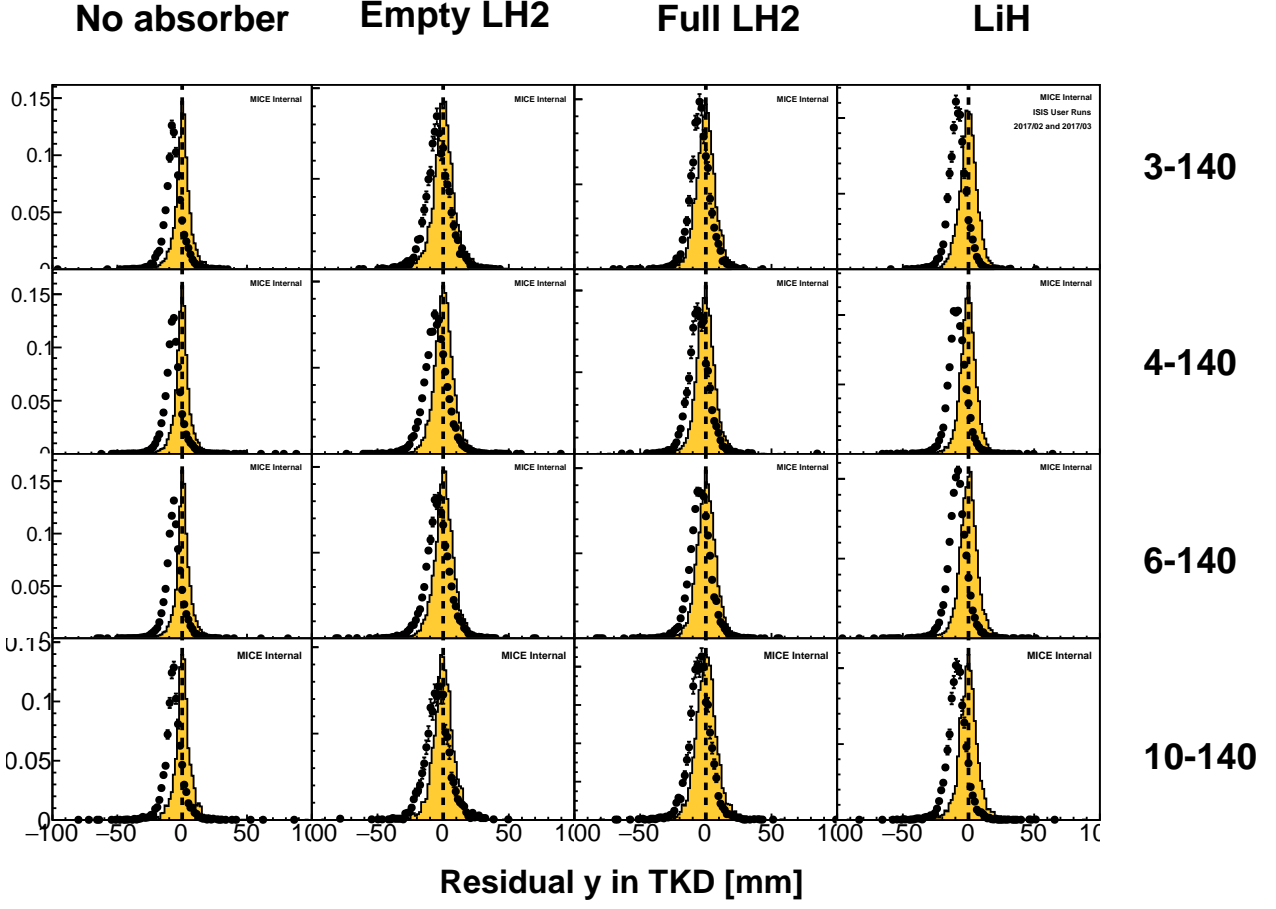


Figure 44: Residual y position of TKU tracks extrapolated to TKD, as compared to the tracks in TKD.

x , α_T , is called pitch, about y , β_T , is called yaw and about z , γ_T , is called roll. For a straight track of local coordinates (x_t, y_t, z_t) at the tracker centre, the global coordinates are reconstructed as

$$\begin{pmatrix} \xi_t \\ v_t \\ \zeta_t \end{pmatrix} = \begin{pmatrix} x_t - \gamma_T y_t + \beta_T z_t + x_T \\ y_t + \gamma_T x_t - \alpha_T z_t + y_T \\ z_t - \beta_T x_t + \alpha_T y_t + z_T \end{pmatrix}. \quad (10)$$

in the first order small angles approximation. The global gradients of the straight track thus read

$$\begin{aligned} \xi'_t &= \frac{d\xi_t}{d\zeta_t} = \frac{dx_t - \gamma_T dy_t + \beta_T dz_t}{dz_t (1 - \beta_T x'_t + \alpha_T y'_t)} \simeq x'_t - \gamma_T y'_t + \beta_T, \\ v'_t &= \frac{dv_t}{d\zeta_t} = \frac{dy_t + \gamma_T dx_t - \alpha_T dz_t}{dz_t (1 - \beta_T x'_t + \alpha_T y'_t)} \simeq y'_t + \gamma_T x'_t - \alpha_T. \end{aligned} \quad (11)$$

There are six potential unknowns per tracker. Some simplifications can be made to lower the amount of unknowns. The z_T coordinate of each tracker is known to great accuracy from the survey. It may also be shown that the roll of the trackers has negligible influence on the alignment and may be ignored [16]. The beam-based detector alignment is critical to find the $(x_T, y_T, \alpha_T, \beta_T)$ constants for each tracker.

The location of the TOFs is used as the reference for the tracker alignment. The line that joins the centre of TOF1 with the centre of TOF2 is chosen to be the reference axis. A deviation from this axis is considered as a misalignment of the trackers. Multiple scattering in the beam line does not allow to do the alignment on single

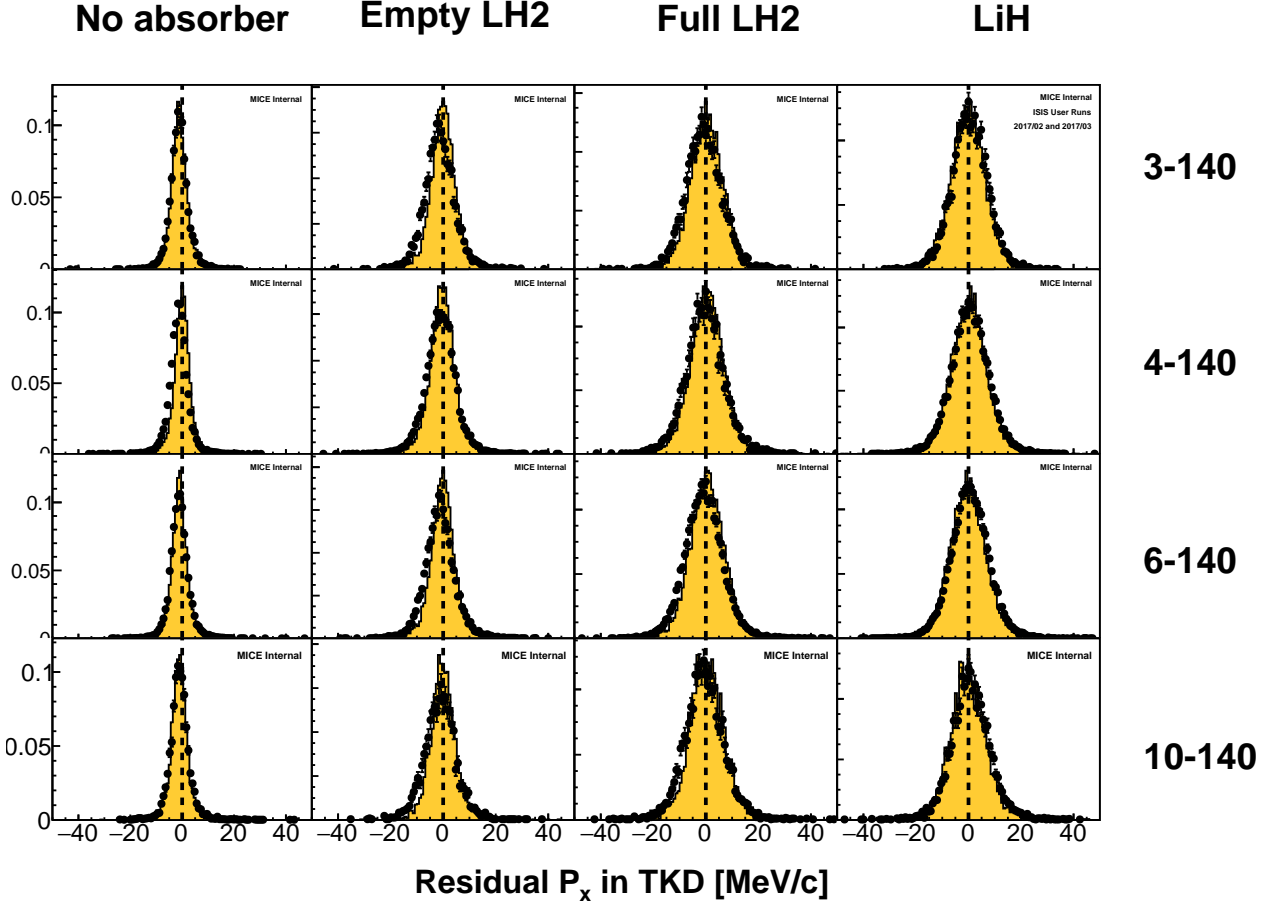


Figure 45: Residual p_x of TKU tracks extrapolated to TKD, as compared to the tracks in TKD.

particle basis but works for a larger sample of particles. The mean residual angles and positions of the trackers with respect to the TOF12 axis are an essential and powerful tool to infer the correction factors. Figure 53 shows the path of a single particle that scatters in the absorber module of the MICE experiment.

Each TOF provides a single space point in the global coordinate system (ξ_i, v_i, ζ_i) with i the ID of the TOF. This position is assumed to be the true position with a large uncertainty due to the limited granularity of the detector ($\sigma_x \sim \sigma_y \sim 17$ mm). The gradients of the track between the two TOFs are reconstructed as:

$$\psi'_{12} = \frac{\psi_2 - \psi_1}{\zeta_2 - \zeta_1}, \quad \psi = \xi, v. \quad (12)$$

The extrapolated position of the TOF reference track in the centre of tracker $t = u, d$ is

$$\psi_{12}^t = \psi_1 + \frac{\psi_2 - \psi_1}{\zeta_2 - \zeta_1} (\zeta_T - \zeta_1) = (1 - \chi_T)\psi_1 + \chi_T\psi_2, \quad \psi = \xi, v, \quad (13)$$

with $\chi_T = (\zeta_T - \zeta_1)/(\zeta_2 - \zeta_1)$, the fractional distance from TOF1 to the tracker centre.

Tracker $t = u, d$ samples the particle track in five different stations (x_t^j, y_t^j, z_t^j) , with $j = 1, \dots, 5$. This allows for the reconstruction of a straight track with gradients x'_t (resp. y'_t) in the xz (resp. yz) projection and its position at the centre, $(x_t, y_t, 0)$. No assumption is made on the prior position of the tracker and hence the coordinates and gradients are returned in local coordinates, i.e. assuming a tracker perfectly aligned with the beam axis, whose centre lies at $z = 0$.

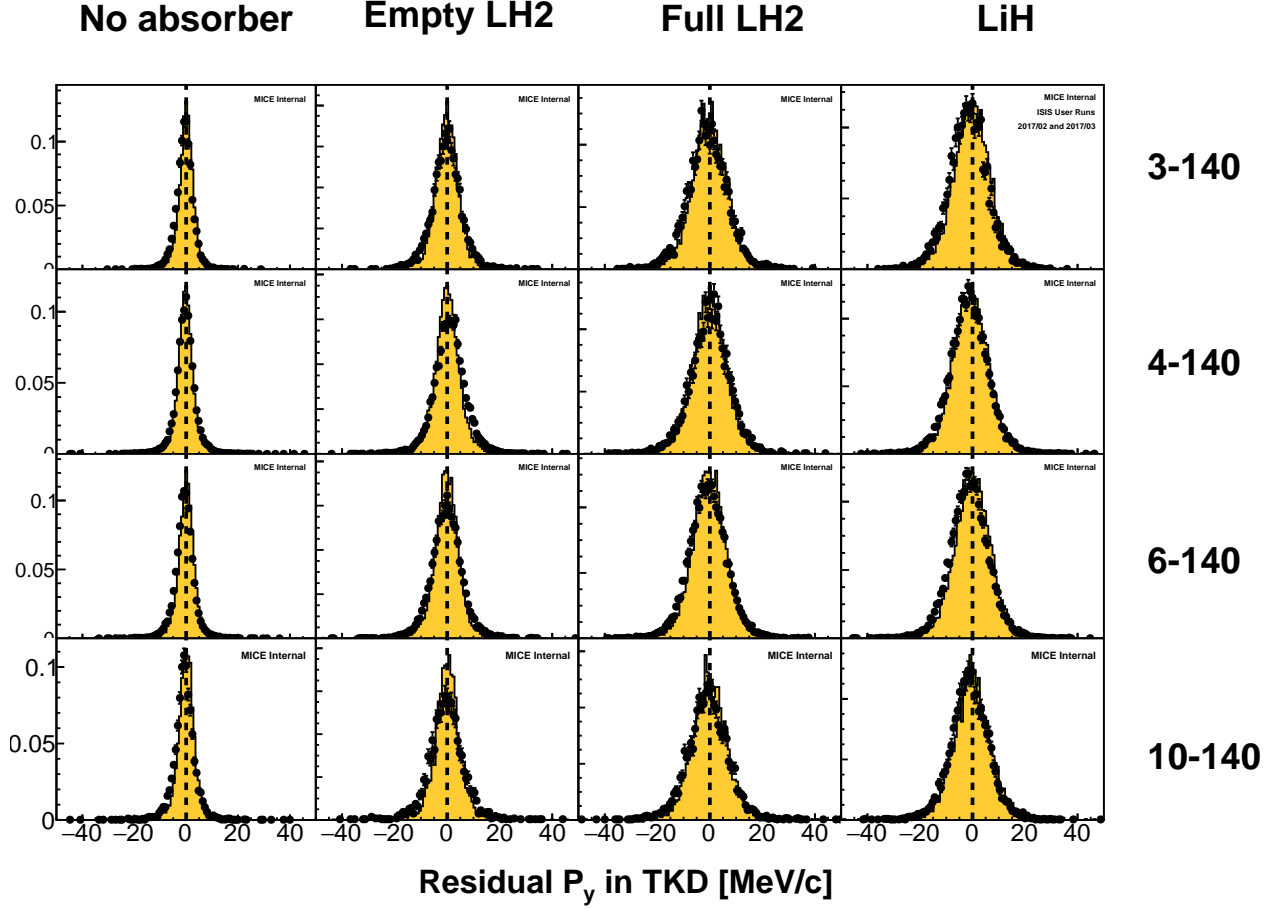


Figure 46: Residual p_y of TKU tracks extrapolated to TKD, as compared to the tracks in TKD.

In global coordinates, on average, the track reconstructed between TOF1 and TOF2 should agree with the track reconstructed in either tracker, i.e. the mean residuals should be zero. Applying this reasoning to the unknown offset and angles yields the following system of four equations with four unknowns [16]:

$$\begin{cases} \langle x'_t - \xi'_{12} \rangle = -\beta_T \\ \langle y'_t - v'_{12} \rangle = \alpha_T \\ \langle x_t - \xi^t_{12} \rangle = -x_T \\ \langle y_t - v^t_{12} \rangle = -y_T \end{cases} . \quad (14)$$

The measurement of four residual distributions per tracker yields the alignment constants.

The method described here assumes that the mean residuals can be measured with great accuracy and, more importantly, are unbiased. A bias in one of the residual distributions inevitably introduces a bias in the measurement of the corresponding alignment parameter, as they are directly proportional. The main source of bias is the scattering in the material between TOF1 and TOF2. If the beam is not perfectly centred, particles preferentially scrape out on one side of the magnet bore, anisotropically curbing a specific tail of the residual distribution. To nullify this effect, a fiducial cut is applied to the upstream sample. Only particles that are expected to be contained in the downstream tracker are included in the analysis [16].

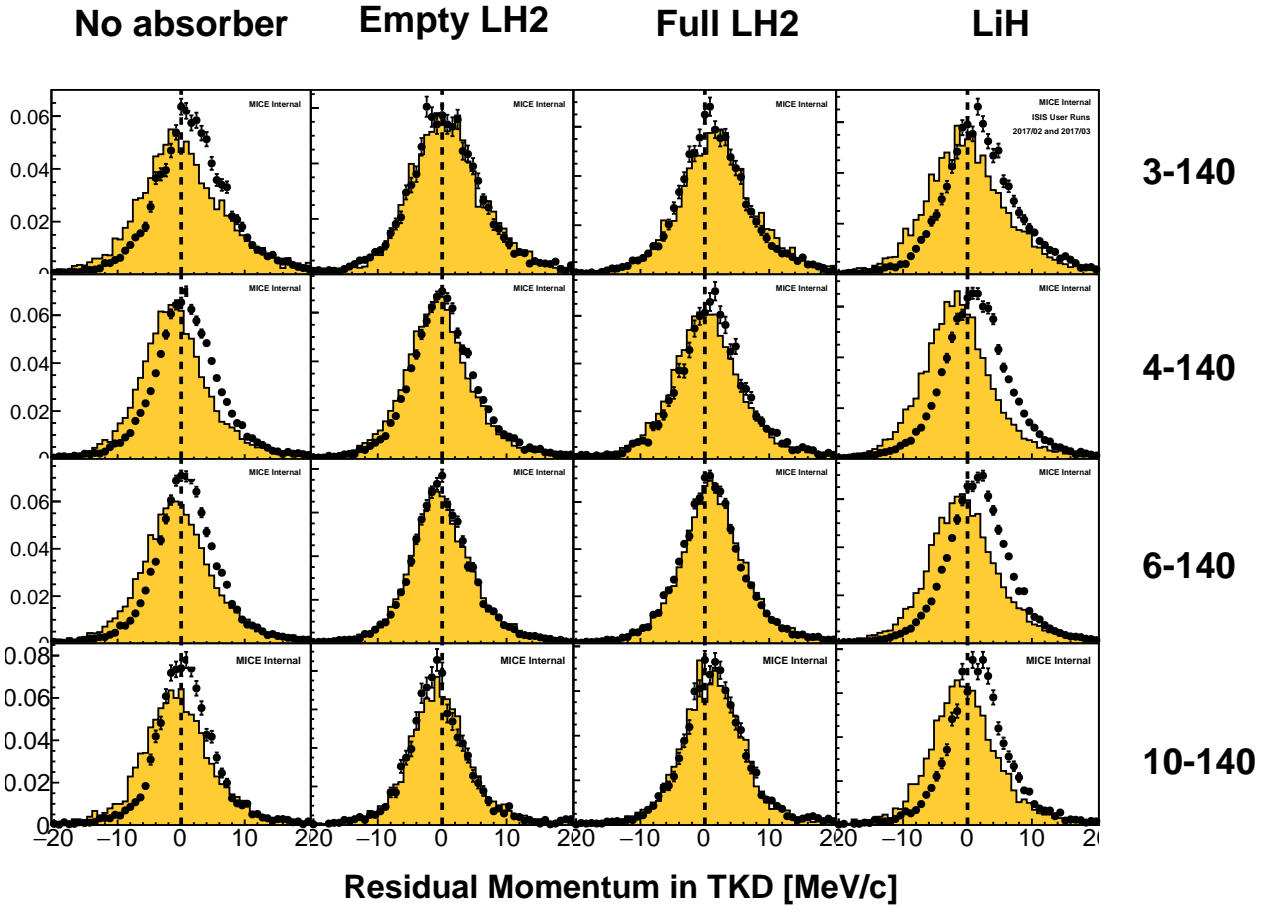


Figure 47: Residual p_{tot} of TKU tracks extrapolated to TKD, as compared to the tracks in TKD.

545 9.3 Alignment of a data sample

Data is recorded with the superconducting magnetic channel of the experiment turned off, i.e. with tracks going in a straight line from TOF1 to the beam dump. High momentum beams are used in order to reduce the RMS scattering angle and maximize transmission. The settings used correspond to ‘pion’ beams of positive polarity to maximize statistics. The beams exhibit a variety of distributions in the beam line. An agreement between the 550 independent fits guarantees an unbiased measurement of the alignment constants.

Provided with the unbiased sample produced as described in section 9.2, each track yields a set of global gradients between TOF1 and TOF2, ξ'_{12} and v'_{12} , and global extrapolated positions at the tracker centres, ξ^t_{12} and v^t_{12} . It also records the position of the track at the centre of the trackers in local coordinates, x_t and y_t , and its local gradients, x'_t and y'_t . The residual distributions necessary to measure the left hand side of 555 equations 14 are produced in order to measure the eight alignment parameters. Figure 54 shows the gradient residuals between y'_u and v'_{12} for run 9367. The mean residual yields the the pitch of the upstream tracker, α_U .

To ensure the best possible fit to the tracker parameters, the algorithm is applied multiple times. The first estimate of $x_T, y_T, \alpha_T, \beta_T$ is used as an input to the sample selection part of the algorithm. The process is repeated until the alignment constants converge. Figure 55 shows the evolution of the optimal upstream tracker 560 pitch, α_U^* , over five iterations for run 9367.

Each data set was processed independently with the algorithm. Figure 56 compiles the alignment parameters

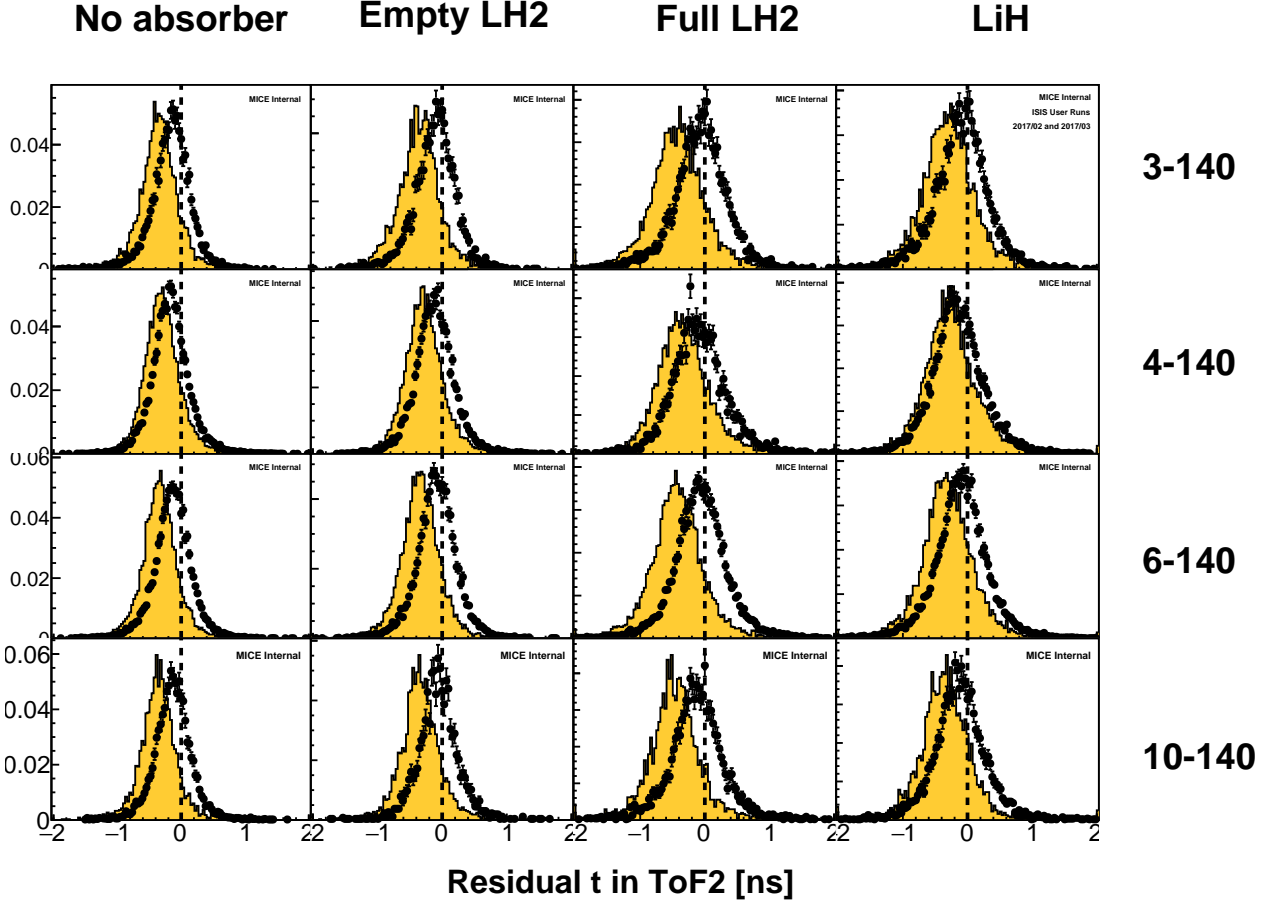


Figure 48: Residual time of TKU tracks extrapolated to ToF2, as compared to the time measured in ToF2. The track times were drawn from ToF1 with appropriate offsets for time-of-flight from TKU to ToF1 considered.

measured for each run. The measurements are in good agreement with one another and show no significant discrepancy. The constant fit χ^2/ndf is close to unity for each fit, which indicates that there are no significant additional source of uncertainty. The optimal parameters are summarised in table 10.

	x [mm]	y [mm]	α [mrad]	β [mrad]
TKU	-0.032 ± 0.094	-1.538 ± 0.095	3.382 ± 0.030	0.412 ± 0.029
TKD	-2.958 ± 0.095	2.921 ± 0.096	-0.036 ± 0.030	1.333 ± 0.030

Table 10: Summary table of the optimal alignment constants measured in the high-momentum straight-track data acquired during the 2017/01 ISIS user cycle.

565 9.4 Propagation

The fitted parameters are used to yield the global track coordinates at the tracker $t = u, d$ centres, (ξ_t, v_t, ζ_t) , through equation 10 and the global gradients ξ'_t, v'_t through equation 11. A corrected global track is propagated in an adjacent detector module M at ζ_m through

$$\psi_t^m = \psi_t + \psi'_t(\zeta_m - \zeta_t), \quad \psi = \xi, v. \quad (15)$$

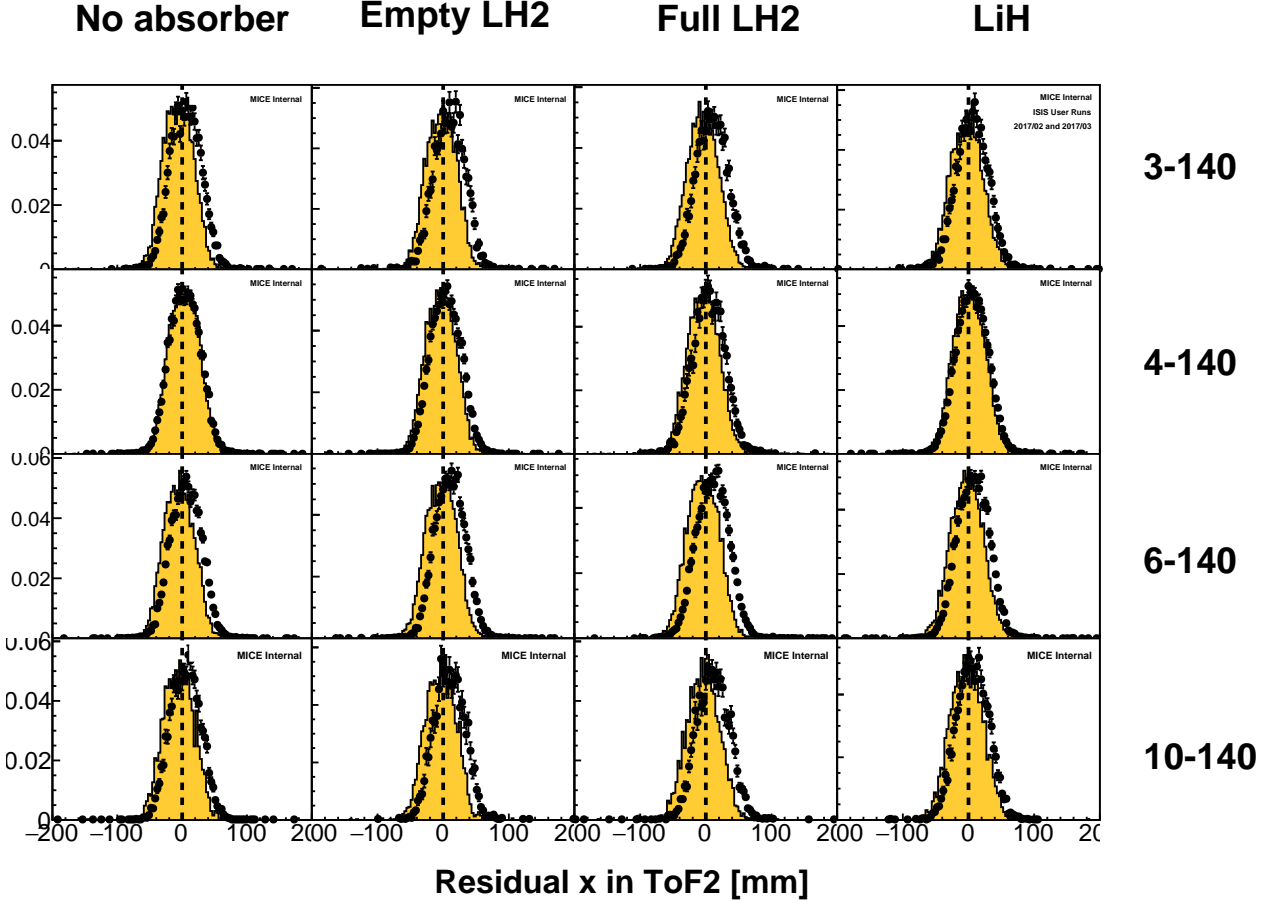


Figure 49: Residual x position of TKD tracks extrapolated to TOF2, as compared to the position measured in TOF2.

Provided exact corrections, a detector module M that measures a global position (ξ_m, v_m, ζ_m) verifies

$$\begin{cases} \langle \psi_m - \psi_t^m \rangle = 0 \\ \langle \psi'_m - \psi'_t \rangle = 0 \end{cases}, \quad \psi = \xi, v. \quad (16)$$

As a consistency check, the tracks are first propagated between the two trackers. The results are shown in figure 57. The top left and right distributions show the residuals between the TKU and TKD tracks at the centre of the downstream tracker and at the level of the absorber, respectively. The bottom two histograms show the agreement between the angles measured upstream and downstream. The azimuthal angle residuals show consistency between the roll of the two trackers.

The upstream tracker tracks are extrapolated into TOF1 and the downstream tracker tracks are propagated into the three downstream particle identification detectors: TOF2, the KL and the EMR. The residual plots are represented in figure 58. The values obtained show good agreement between the tracks and the space points measured in other MICE detectors.

Special care is taken when evaluating the central value of the residual distributions. The two trackers and the Electron-Muon Ranger have a sufficient spacial resolution to follow a near-Gaussian distribution. The residuals involving these detectors are fitted with a standard multivariate normal of mean μ and width σ between the two half-maximum, i.e. in the range $\mu \pm 1.1775 \sigma$. The TOF hodoscopes and the KL do not have a sufficient

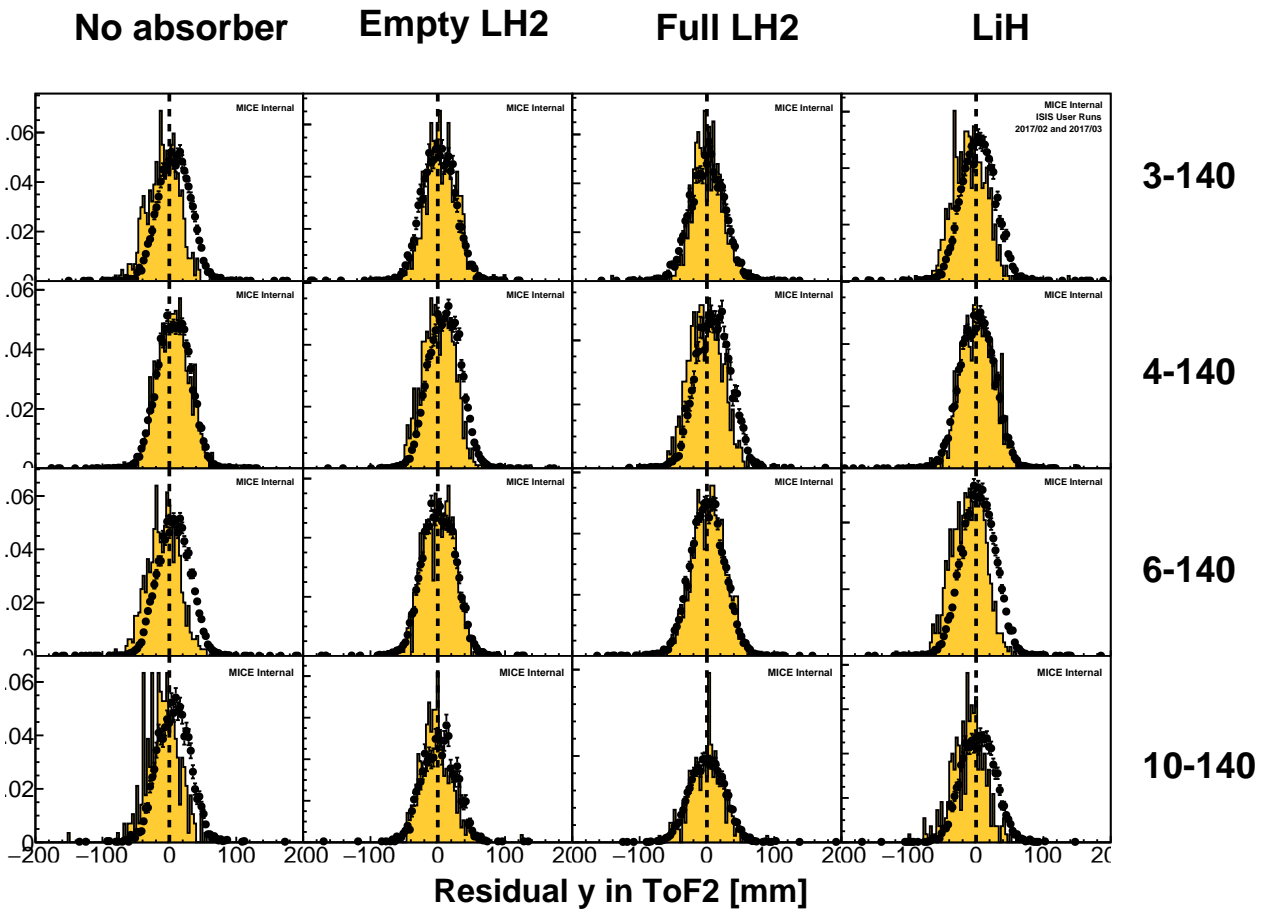


Figure 50: Residual y position of TKD tracks extrapolated to TOF2, as compared to the position measured in TOF2.

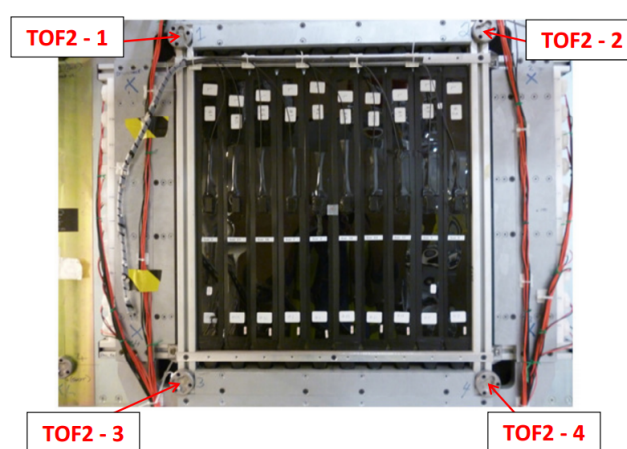


Figure 51: Picture of the TOF2 time-of-flight hodoscope and its four survey monuments labelled TOF2.1–2.4.

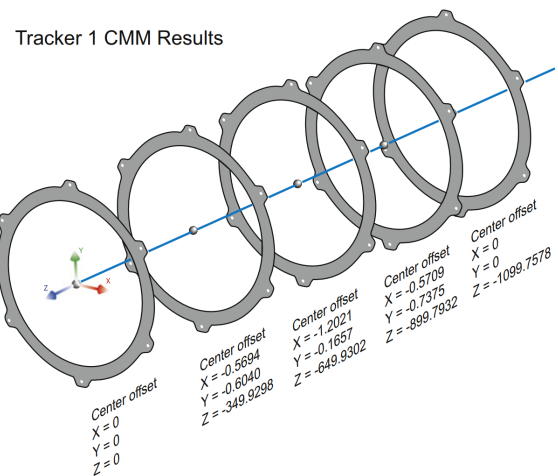


Figure 52: Disposition of the downstream tracker stations along with the CMM measurements of their position with respect to the reference axis.

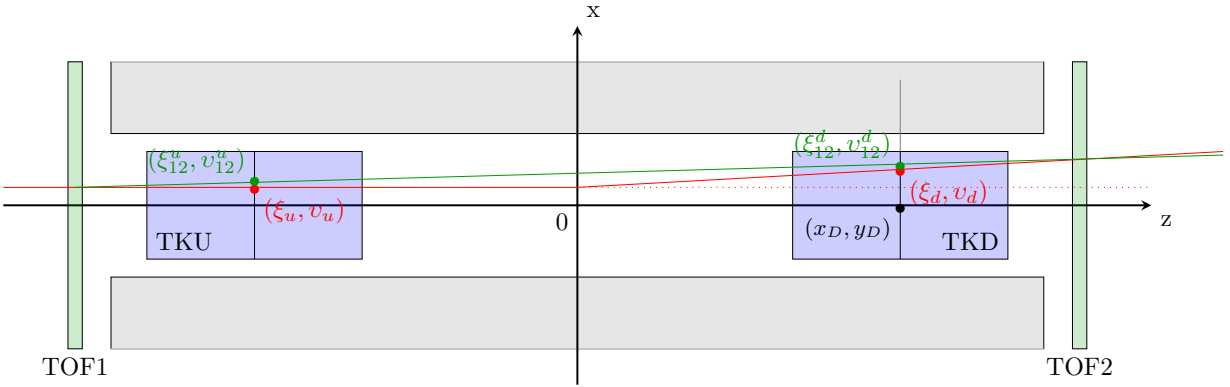


Figure 53: True path of a single particle track (red) and its path as reconstructed from the time-of-flight system (green). The position of the track at the tracker centres is represented by markers.

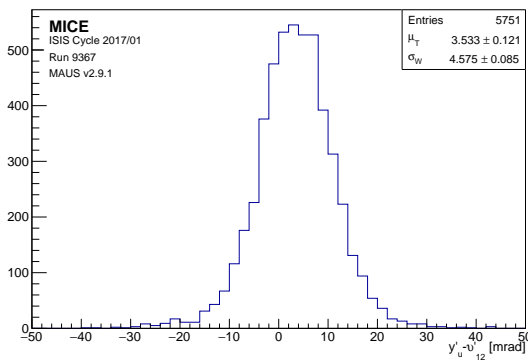


Figure 54: Residuals distribution between the pitch gradients measured locally in TKU, y'_u , and globally between TOF1 and TOF2, v'_{12} .

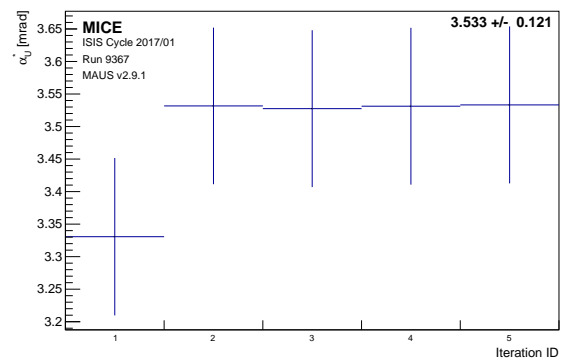


Figure 55: Evolution of the optimal value of the pitch angle in TKU, α_U^* , for different number of iterations of the fitting algorithm.

resolution to produce residuals that follow a Gaussian distribution. A probability density function of the form

$$h(x) = \frac{1}{4W} \left(\tanh \left[\frac{x - \mu + W}{\sigma} \right] - \tanh \left[\frac{x - \mu - W}{\sigma} \right] \right) \quad (17)$$

is used in each projection to fit the residuals involving the low granularity detectors. The constant μ represents the central value of the residual distribution, σ the residual width and W the half-width of one of the low-resolution detector pixel. The parameters obtained for each of the fits are represented on the residual graphs. The values found for W are consistent with pixels of 6 cm in TOF1 and TOF2 and of 4.4 cm in the KL.

10 Absorber

As a muon beam passes through material, some of the kinetic energy of the muons is lost through ionization of the material. This process results in a reduction of the normalised transverse emittance and the beam is said to be cooled. Muons will also undergo multiple Coulomb scattering which increases the divergence of the beam, thereby increasing the normalised transverse emittance and heating the beam.

Ionization-energy loss is characterised by $\frac{dE}{dx}$, where E is the muon energy and x is the distance travelled within the absorber. Multiple Coulomb scattering is characterised by the radiation length, X_0 . For liquid

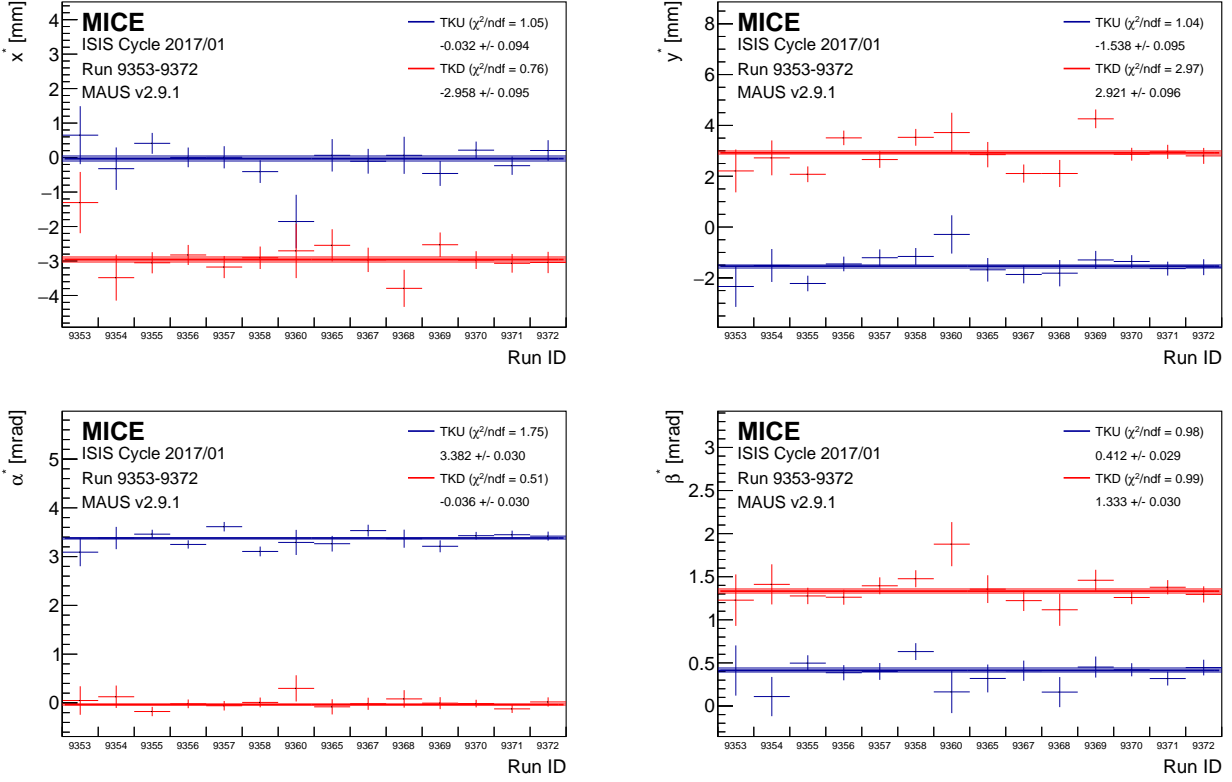


Figure 56: Consistency of the alignment algorithm across runs acquired during the 2017/01 ISIS user cycle.

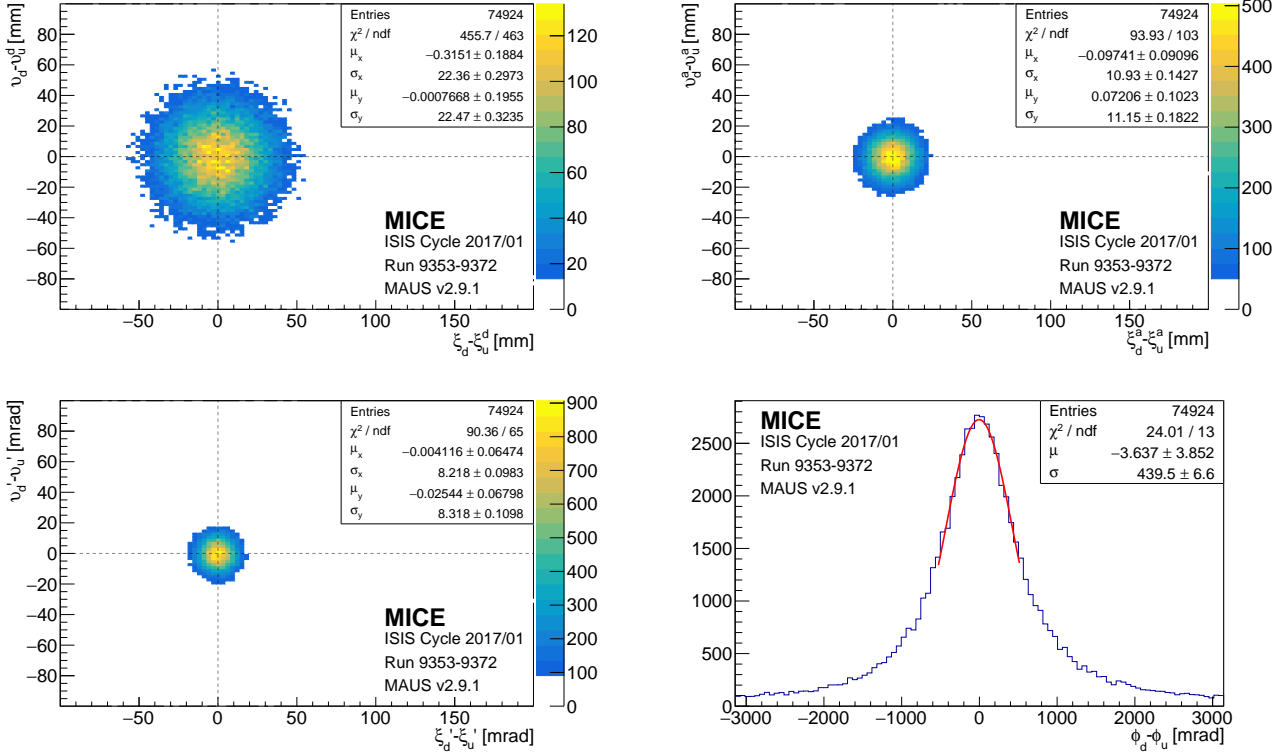


Figure 57: Tracker-to-tracker residual distributions in position (**top**) and angle (**bottom**).

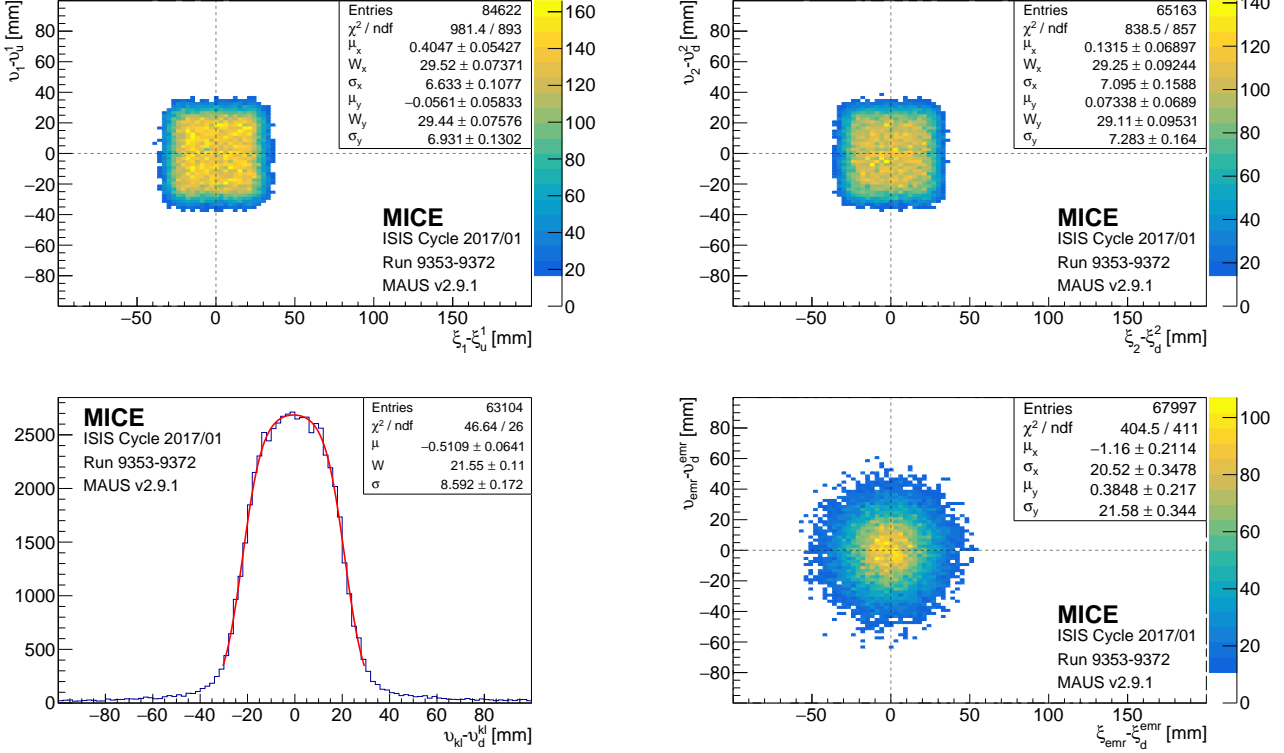


Figure 58: Tracker to particle identification detectors residual distributions (TOF1, TOF2, KL and EMR).

hydrogen, $\frac{dE}{dx} \sim 0.03 \text{ MeV/mm}$ and $X_0 \sim 8905 \text{ mm}$ [17]. The absorber vessel was manufactured using aluminium for which $\frac{dE}{dx} \sim 0.4 \text{ MeV/mm}$ and $X_0 \sim 90 \text{ mm}$ [17]. To maximise the cooling effect from energy loss in liquid hydrogen, while minimising the heating effect from multiple Coulomb scattering in the aluminium windows, these windows were required to be as thin as possible.

Figure ?? shows the drawings of the absorber focus coil (AFC) module and the installed absorber vessel. The absorber vessel was set at the centre of the FC magnet coils. Safety considerations required a secondary containment system. Therefore, the absorber vessel was situated in an evacuated space within two more thin aluminium safety windows, so the muon beam had to traverse four windows, as shown in the left panel in Figure ??.

geometry definition and validation.

10.1 Absorber vessel body

The absorber vessel comprised a cylindrical aluminium body sealed with two thin aluminium end windows, as shown in the right panel of figure ???. The absorber vessel was specified to contain 22 l of liquid, so the body had an inner diameter of 300 mm and a length between its end flanges of 230 mm. The length along the central axis between the two domes of the thin aluminium end windows was 350 mm. The body contained an annular cooling channel within its walls that could act as a heat exchanger. This channel was designed to allow the possibility of cooling the vessel body directly using liquid nitrogen, or even liquid helium. However, it was found that this cooling was not necessary because the absorber vessel cooled sufficiently quickly with cold gas from the condenser, as described in section ???. Small indium-sealed flanges connected the aluminium pipes from the absorber vessel to the stainless-steel pipes from the condenser.

Figure 59 shows a photograph of the inside of the absorber vessel body. The two flanged windows were sealed

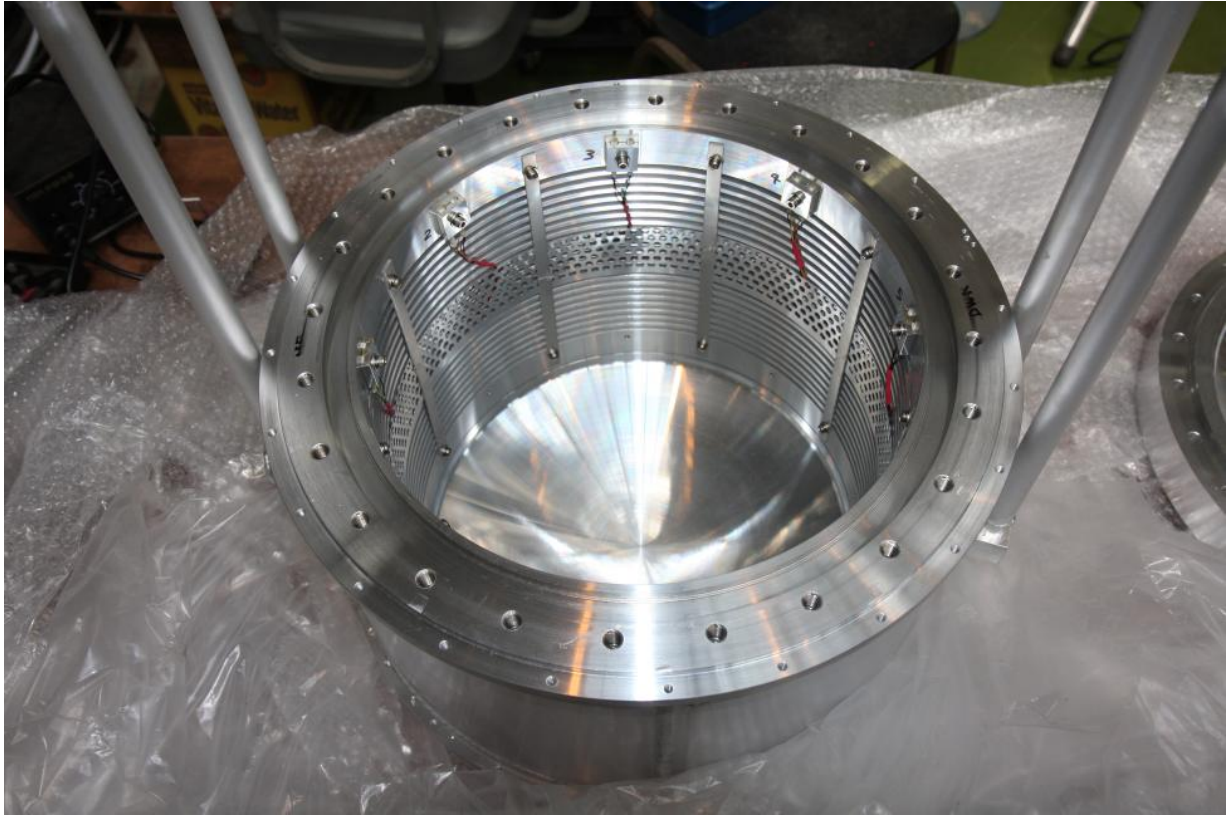


Figure 59: Photograph of the absorber vessel body.

to the end flanges of this body using indium contained in grooves. The heat exchanger fins and five pairs of thermometers (LakeShore Cernox 1050-SD) are visible in this photograph. These five thermometer pairs were inside the vessel at locations spaced by 45° around the circumference and were monitored with a LakeShore 218S. Each pair monitored the presence of liquid hydrogen at that position; one of these Cernox sensors was operated with a small current as a thermometer, and the other was occasionally heated by a pulse of larger current. The difference between the two measured temperatures was small when these sensors were in liquid due to good cooling efficiency, but the difference was larger when these sensors were in gas since heat transport through the gas is worse than in the liquid. The sensor wires were extracted to vacuum part-way along the liquid-hydrogen inlet pipe at a 30-pin hermetic feed-through, as shown in figure ???. Signals from each sensor were carried on two wires inside the absorber vessel, between the sensor and the feed-through, and by four wires in the vacuum outside the vessel. Two Cernox thermometers and two heaters (LakeShore HR-25-100) were mounted externally on each end flange. Two additional Cernox thermometers were mounted externally on the hydrogen inlet and outlet lines. These thermometers were exposed to vacuum and thermal radiation so the thermometry here was less accurate than that inside the absorber vessel, but gave indications of the flow of cooling gas in the circuit. To minimise heat input from contact with the magnet bore, the absorber vessel was mounted on glass-epoxy (G10) supports of low thermal conductivity. To minimise radiative heat input, multilayer insulation (MLI) was wrapped around the absorber vessel and all the low-temperature pipework. The number of layers of MLI over the end windows was first entered into a Monte Carlo program to check that the scattering of muons by the MLI was insignificant compared to that of the windows, before the vessel was integrated into the system and cooled.

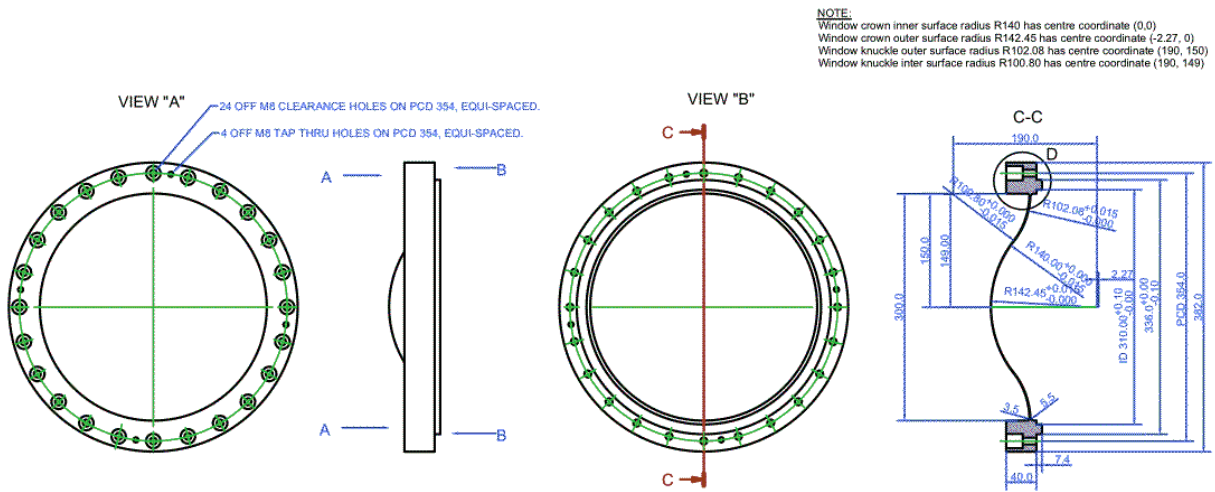


Figure 60: Aluminium absorber vessel window with a central thickness of $180 \mu\text{m}$ for the containment of liquid hydrogen. Both types of safety windows were similar to the vessel window, but had a central design thickness of $210 \mu\text{m}$.

10.2 Windows

The liquid hydrogen was contained between two aluminium windows, each having a thickness of $180 \mu\text{m}$ at the centre and increasing to $360 \mu\text{m}$ near the outer flange. Aluminium safety windows, each with a central thickness of $210 \mu\text{m}$, enclosed the absorber vessel in the magnet bore. Thin aluminium was chosen to minimise multiple scattering. Thinner windows lead to less scattering and more muon-beam cooling. Although a MICE window with a central thickness of $125 \mu\text{m}$ had successfully been machined using alloy 6061-T651, it would not withstand enough pressure. The pressure in the absorber vessel reached 1500 mbar during typical operations. The aluminium alloy we chose to use (6061-T651) was assayed to contain 0.61% silicon, 0.26% iron, 0.25% copper, 0.02% manganese, 1.02% magnesium, 0.20% chromium, 0.01% zinc, 0.05% titanium, 0.01% zirconium, 0.15% maximum other material, and at least 97.42% aluminium (all measured by weight). The yield strength was measured at room temperature to be $39,900 \pm 700 \text{ psi}$ ($275 \pm 5 \text{ MPa}$), although this would be greater at 20 K. A drawing of a MICE absorber vessel window is shown in figure 60. The double-bend geometry increases the burst strength.

10.2.1 Window manufacture

A CNC Fadal 5020A vertical machining centre and a CNC Romi lathe with a 27 inch swing were used to machine the windows from a solid block of aluminium alloy. Precision backing plates supported the windows during this process. Each window was machined to a $2000 \mu\text{m}$ central thickness, and then measured with the micrometer jig shown in figure 63. The window was then returned to the lathe for final machining while the lathe still had the positions stored in its memory. Clear plastic cases were fabricated to protect the windows from damage in transit, while still allowing visual inspection. Finished windows can be seen in figures 61 and 64.

Table 11: Results of measuring the central thickness of the three types of windows with the View Precis 3000 Optical CMM shown in figure 61. The windows actually used in MICE were numbers 002, 003, 009, and 014.

Window #	Window Type	Central Thickness Measured (μm)	Central Thickness Design (μm)	Note
001	Absorber		180	
002	Absorber	174 ± 5	180	
003	Absorber	184 ± 2	180	
004	Absorber		180	
005	Absorber	176 ± 6	180	
006	Safety I	222 ± 6	210	flaw at centre
007	Safety I		210	flaw at centre
008	Safety II	233 ± 5	210	
009	Safety II	230 ± 9	210	
010	Absorber		180	
011	Absorber		180	
012	Safety I	197 ± 7	210	
013	Safety I		210	
014	Safety I	197 ± 8	210	

10.2.2 Window thickness measurement

The thicknesses of three different types of finished windows (one absorber and two safety) were measured with the View Precis 3000 Optical Co-ordinates Measurement Machine (CMM) shown in figure 61. The complete surface profile of a window was measured with the laser on one side, and then the window was turned over to measure the other side. The difference between the surface profiles of both sides of the window gave the thickness. Three tuning balls were glued to the window to establish the reference coordinate system; key to getting a good measurement was to establish the same reference coordinate system for both sides of each window. Some results of the measurements are shown in table 11 and figure 62. For some of the windows, the thickness measurement was checked by scanning only the small area around the window centre with a very dense meshing. This gave a more accurate measurement of the thickness at the window centre.

Low energy electrons are strongly attenuated by modest thicknesses of aluminium. Two different beta sources, ^{90}Sr and ^{204}Tl , were used to measure the thickness of a MICE window. The source and detector (Geiger tube) were on opposite sides of the window so there was no need to move the window during this process, as was required with the laser CMM. The attenuation of electrons in a thin sheet of material of thickness x was described using the equation:

$$R = A e^{\alpha x} + B e^{\beta x} + C. \quad (18)$$

The apparatus was optimised to measure the central window thickness by choosing beta sources with electron energies that have a half-range of about $180 \mu\text{m}$ in aluminium. Due to electron scattering, the result can be sensitive to apparatus geometry so a careful calibration was performed using aluminium sheets of known thickness with counts being accumulated for 10 minutes per sheet. The central thickness of the absorber window in figure 64 was measured to be 178 ± 6 (stat) ± 4 (fit) μm .



Figure 61: The View Precis 3000 Optical CMM measured the surface profile of each window, one side at a time.



Figure 62: Result of the CMM measurement of one side of one window. All the axes are labelled in units of millimetres.



Figure 63: Jig for measuring window thickness at the centre and at 15° from the peak of the dome with a pair of Starrett T465 micrometers accurate to 3 microns.



Figure 64: ^{90}Sr and ^{204}Tl beta sources and a Geiger tube were used to check the central thicknesses of windows.



Figure 65: This absorber vessel window burst when pressurised with water.



Figure 66: This Type I safety window (number 012 in Table 11) burst when slowly pressurised with nitrogen gas.

10.3 Validation of the absorber model in MAUS

11 Conclusions

665 To be written at last.

References

- [1] M. Bonesini, “The design of MICE TOF0 detector,” *MICE Note 145* (2006) .
<http://mice.iit.edu/micenotes/public/pdf/MICE0145/MICE0145.pdf>.
- [2] R. Bertoni *et al.*, “The construction and laboratory tests for MICE TOF0/1 detectors,” *MICE Note 241* (2008) . <http://mice.iit.edu/micenotes/public/pdf/MICE0241/MICE0241.pdf>.
- [3] R. Bertoni, A. Blondel, M. Bonesini, G. Cecchet, A. de Bari, J. S. Graulich, Y. Karadzhov, M. Rayner, I. Rusinov, R. Tsenev, S. Terzo, and V. Verguilov, “The design and commissioning of the MICE upstream time-of-flight system,” *Nuclear Instruments and Methods in Physics Research A* **615** (Mar., 2010) 14–26, arXiv:1001.4426 [physics.ins-det].
- [4] R. Bertoni *et al.*, “The construction of the MICE TOF2 detector,” *MICE Note 286* (2010) .
<http://mice.iit.edu/micenotes/public/pdf/MICE0286/MICE0286.pdf>.
- [5] D. Rajaram and V. C. Palladino, “The Status of MICE Step IV,”.
<http://accelconf.web.cern.ch/AccelConf/IPAC2015/papers/thpf122.pdf>.
- [6] M. Bonesini, “Progress of the MICE experiment,” arXiv:1510.08825 [physics.acc-ph].
- [7] The MICE Collaboration, “Characterisation of the muon beams for the Muon Ionisation Cooling Experiment,” *ArXiv e-prints* (June, 2013) , arXiv:1306.1509 [physics.acc-ph].
- [8] D. Adams *et al.*, “Pion contamination in the MICE muon beam,” *Journal of Instrumentation* **11** (Mar., 2016) P03001, arXiv:1511.00556 [physics.ins-det].
- [9] M. A. Rayner, *The development of a novel technique for characterizing the MICE muon beam and demonstrating its suitability for a muon cooling measurement*. PhD thesis, Oxford U., 2011.
<http://lss.fnal.gov/archive/other/thesis/rayner-m.pdf>.
- [10] Y. Karadzhov *et al.*, “TOF detectors Time Calibration,” *MICE Note 251* (2009) .
<http://mice.iit.edu/micenotes/public/pdf/MICE0251/MICE0251.pdf>.
- [11] L. Cremaldi *et al.*, “Progress on Cherenkov Reconstruction in MICE,” *MICE Note 473* (2015) .
<http://mice.iit.edu/micenotes/public/pdf/MICE0473/MICE0473.pdf>.
- [12] R. Asfandiyarov *et al.*, “The design and construction of the MICE Electron-Muon Ranger,” *Journal of Instrumentation* **11** (Oct., 2016) T10007, arXiv:1607.04955 [physics.ins-det].
- [13] F. Drielsma, “Electron-Muon Ranger: hardware characterization,” Master’s thesis, University of Geneva, 2014. <https://arxiv.org/abs/1710.06946>.
- [14] D. Adams *et al.*, “Electron-muon ranger: performance in the MICE muon beam,” *Journal of Instrumentation* **10** (Dec., 2015) P12012, arXiv:1510.08306 [physics.ins-det].
- [15] F. Drielsma, *Measurement of the Increase in Phase Space Density of a Muon Beam through Ionization Cooling*. PhD thesis, University of Geneva, 10, 2018.
- [16] F. Drielsma, “Beam-based detector alignment in the MICE muon beam line,” arXiv:1805.06623 [physics.ins-det]. <https://arxiv.org/abs/1805.06623>.
- [17] **Particle Data Group** Collaboration, M. Tanabashi *et al.*, “Review of particle physics,” *Phys. Rev. D* **98** (Aug, 2018) 030001. <https://link.aps.org/doi/10.1103/PhysRevD.98.030001>.